Coupling between a coherent structure and fine-scale turbulence

Mogens V. Melander
Department of Mathematics, Southern Methodist University, Dallas, Texas 75275-0156

Fazle Hussain
Department of Mechanical Engineering, University of Houston, Houston, Texas 77204-4792
(Received 8 January 1993; revised manuscript received 3 May 1993)

Our direct numerical simulations show that a coherent structure ($\mathcal{C}$) in an initially fine-scale homogeneous, isotropic turbulent field breeds secondary structures in its vicinity. These are organized. Shaped like concentric spiral threads perpendicular to the axis of $\mathcal{C}$, each is found to be highly polarized with the azimuthal vorticity component being dominant. The threads occur in pairs, and the polarization typically alternates between adjacent threads. Above a critical value (≈ 1000) of $\mathrm{Re} \equiv \Gamma_{\mathcal{C}}/\nu$ ($\Gamma_{\mathcal{C}}$ is circulation, ν is kinematic viscosity) a small number of circulation-rich threads emerge as a result of the evolution. The secondary structures are of both practical and theoretical importance. For $\mathrm{Re} > \mathrm{Re}_{\mathrm{crit}}$, the strongest threads excite bending waves on the axis of $\mathcal{C}$. For $\mathrm{Re} \gg \mathrm{Re}_{\mathrm{crit}}$, $\mathcal{C}$ is eventually destroyed. We believe that this feedback phenomenon is of critical importance for the rearrangement of coherent structures (CS) and transition to turbulence in shear flows such as plane, circular, and elliptic jets. Turbulent mixing near $\mathcal{C}$ is due to entrainment and ejection of fluid by the threads. Local isotropy assumption cannot be applied near a CS, because our results show anisotropy in a layer surrounding $\mathcal{C}$. The threads are shown to be the combined result of three mechanisms: (1) azimuthal alignment of small-scale vorticity by the strain rate field of $\mathcal{C}$; (2) merger (pairing) and axisymmetrization as in two-dimensional turbulent flows, enabled by the alignment; and (3) polarization by differential rotation.

PACS number(s): 47.27.−i

I. INTRODUCTION

The interactions between large and small scales is of fundamental importance for a deeper understanding of the physics of turbulent flows and their modeling, and for developing effective techniques for the control of turbulence phenomena. This is particularly true for flows featuring large-scale coherent structures. In such flows, for that matter in any turbulent shear flow, it is questionable if the small scales are statistically isotropic; i.e., we have had lingering doubts about the validity of *local isotropy,* which is the centerpiece of Kolmogorov's theory and is still the breeding ground for theories of turbulent flows. For example, Hussain [1] speculates that in spite of wide-scale separation, large- and fine-scale motions are intimately coupled and that the presence of coherent structures may thus partially cripple the traditional statistical turbulence models, which assume local isotropy. Here we examine this issue further by studying direct numerical simulations of a single idealized coherent structure embedded in a sea of random, small-scale, isotropic turbulence.

The interaction between coherent structures and small scales is difficult to model. On the one hand, a coherent structure generates a local shear, which, if sufficiently strong, can sustain turbulent fluctuations by shear production via alignment and stretching of the fine-scale vorticity. Such turbulent fluctuations can even be generated by a coherent structure itself through various cascade mechanisms, e.g., filamentation, tearing, and reconnection [2]. In the neighborhood of a coherent structure, the small-scale fluctuating vorticity in addition to being stretched is also advected around the coherent structure. On the other hand, the small scales may significantly influence and change the evolution and internal dynamics of the coherent structure itself. A prime example of this phenomenon is the axisymmetrization of a noncircular vortex in two-dimensional (2D) turbulence [3]. Here the small-scale structures (filaments generated by the vortex) influence the large scales (the vortex) in such a way as to make it circularly symmetric. Throughout the history of turbulence research there has been a strong temptation to model the small-scale influence on the large scales by means of a turbulent diffusion mechanism, e.g., mixing lengths, eddy viscosities, as well as sophisticated models such as renormalized-group theory (RNG). In two dimensions, such approaches have been clearly defeated through the discovery that the small scales can self-organize into increasingly larger scales [4]. The 2D mechanism responsible for this inverse energy cascade is pairing, or merger, of vortices. The vortices resulting from successive mergers invalidate statistical theories based on random phases [5].

Similar amalgamation of circulation through frequent vortex mergers is in general not expected to occur in 3D for the geometrical reason that the vorticity vectors lack a preferred direction. However, some 3D turbulent flows are quasi two dimensional in the large scales, e.g., mixing layer, plane jet, near field of a circular jet, and in such flows the amalgamation of circulation through successive pairings is well known [6,7]. In fact, the coherent-structure concept was formulated through an experimental investigation of a mixing layer [8] and the near field of a circular jet [9]. In this paper, we show that the pres-

ence of a large-scale coherent structure imposes preferred direction to the nearby small scales. We examine in detail the spiral structure of the intermittency thus induced by the coherent structure. Our study leads us to formulate a conjecture about local anisotropy of the small scales and internal intermittency in the high-Reynolds-number limit. Also, we investigate the feedback (or backscatter) of the small scales on the coherent vortex and whether this feedback can be modeled by an enhanced diffusion. The similarities as well as differences between the internal intermittency described here and related types [10,11] reported in the literature are discussed in Sec. VIII B.

II. INITIAL CONDITIONS AND THEIR MOTIVATION

The rectilinear laminar vortex (case $L1$) discussed in a companion study [12] has a sinusoidal core-size variation along the axis. This vortex clearly qualifies as a coherent structure. Our numerical simulations (spectral in a periodic box) of the interactions between large and small scales consist of this single dynamically evolving coherent structure embedded in a background flow, which initially consists of random solenoidal fine-scale isotropic velocity fluctuations. Thus there is no interaction with other coherent structures and no self-induced transverse displacement; moreover, the coherent structure dynamics are represented entirely by the core dynamics, whose laminar version we have analyzed in considerable detail elsewhere [12,13]. This idealized setup allows us to focus directly on the large-scale–small-scale coupling and may also be thought of as a model of a segment of a coherent structure (Fig. 1) in turbulent shear flows like jets, wakes, and mixing layers, or of internal intermittency near a rodlike vortical structure.

The initial turbulent background is isotropic, homogeneous, and consists only of scales represented by wave numbers in a certain interval, i.e., $|\mathbf{k}| \in [k_l, k_h]$. Within this interval, the phases are random with a uniform probability distribution, while the amplitudes are random with a C^∞ probability distribution $\mathcal{P}$ times a normalization factor. The normalization factor serves to give the turbulent velocity field a specified rms value u'_{rms}. The distribution $\mathcal{P}$ is

$$\mathcal{P}(\chi)=\begin{cases} 1-\exp\left[\left[\dfrac{2.56}{\chi}\right]\exp\left[\dfrac{1}{\chi-1}\right]\right], & 0\le\chi<1 \\ 0, & 1\le\chi \end{cases} \tag{1}$$

where $\chi=|2|\mathbf{k}|-(k_h+k_l)|/(2k_h-2k_l)$. The graph of $\mathcal{P}$ is flat topped with smoothed flanks [3]. (Note that the use of this distribution makes it easy to redo our simulations at different resolutions.) Thus the turbulent background is herewith specified by k_l, k_h, and u'_{rms}. The motivation for the specific values of these parameters is presented below.

In spite of our idealized setup, the spatial resolution imposes severe restrictions. In order to have a well-resolved calculation, the small scales must necessarily be subject to strong damping. Consequently, the rms value of the small-scale fluctuations must be initially substantial for them to survive in strength for a reasonable length of time and thus be able to dynamically interact with the vortex. We performed a number of preliminary low-resolution (64^3) calculations in order to find the interesting fluctuation levels. In these test runs the background fluctuations consisted of white noise. Even though the fluctuation level always decayed rapidly, we observed the formation of increasingly larger scales in the background, albeit sometimes at very low amplitudes. Simple viscous decay obviously produces a growing scale in the turbulent background; i.e., the larger scales in the white noise dissipate slower than the smaller ones. However, the small-scale-structure dynamics in the meridional planes appeared to have some resemblance with the organization in 2D turbulence. In order to check for a possible small-scale-organization mechanism other than simple viscous decay, we performed a simulation with a turbulent background consisting only of the smallest possible scales allowed by the resolution. The formation of increasingly larger scales in the background occurred also under these conditions, thereby drawing our interest to internal intermittency and small-scale organization.

This then motivates the choice of the random backgrounds listed in Table I, each of which features a spectral gap in wave number between coherent and incoherent scales. Four low-resolution simulations ($T1-T4$) with varying amplitude β of the initial random velocity fluctuations were performed so as to cover the interesting range of β. In case $T1$, the coherent structure emerged in axisymmetric shape after the initial decay of the random fluctuations. In cases $T2$ and $T3$, the

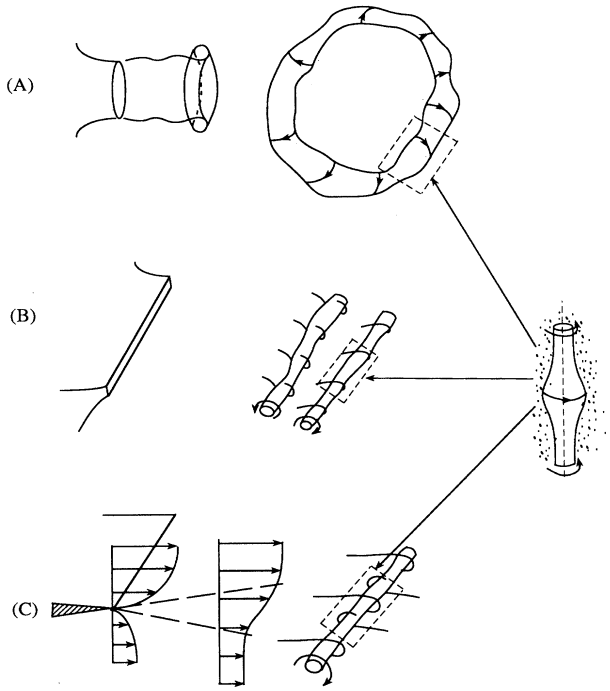

FIG. 1. Sketch of a segment of a coherent structure in some prototypical shear flows. (A) Circular jet; (B) plane jet; (C) mixing layer.

TABLE I. Parameters for simulations (dimensional units). Here N^3 is the spatial resolution; ν is the kinematic viscosity; r_0, μ, and λ describe the initial coherent vortex (i.e., the vortex boundary is given by $s^*(z^*)=r_0^*[1-\mu\cos(2\pi z^*/\lambda^*)]$; ω_0^* is the initial peak vorticity of the coherent vortex; $[k_l,k_h]$ is the interval of wave numbers for the fine-scale turbulence; $\beta=u'_{\rm rms}/\bar{u}_{\rm peak}$ with $\bar{u}_{\rm peak}$ being the peak velocity in the laminar vortex).

Case	N	$10^3\nu$	μ	r_0^*	λ^*	ω_0^*	k_l	k_h	β
$L1$	64	7.563	0.5	0.6	2π	20			0
$T1$	64	7.563	0.5	0.6	2π	20	18	21	0.1
$T2$	64	7.563	0.5	0.6	2π	20	18	21	0.5
$T3$	64	7.563	0.5	0.6	2π	20	18	21	1.25
$T4$	64	7.563	0.5	0.6	2π	20	18	21	2.5
$T5$	128	1.891	0.5	0.6	2π	5	30	34	1.
$T6$	128	1.891	0.5	0.6	2π	5	30	34	2.5
$T7$	128	0.503							
$T8$	128	a							
$T9$	128	0.503							
$T10$	128	a							

[a]In these simulations an artificial viscosity of the form $\nu_4\Delta^2$ is employed, with $\nu_4=1.563\times10^{-6}$.

TABLE II. Parameters for simulations (nondimensional units). The nondimensional values are obtained by using characteristic time and length scales ($\tilde{t}$ and $\tilde{L}$) derived from the initial coherent vortex. $\tilde{t}\equiv8|M^*|/\Gamma^{*2}$ and $\tilde{L}\equiv|8M^*/\Gamma^*|^{0.5}$, where Γ^* is the circulation and M^* is the average axial angular impulse (see [12] for details). Using these units we have $\mathrm{Re}\equiv\Gamma^*/\nu=\tilde{L}^2/\tilde{t}\nu$.

Case	N	Re	μ	r_0	λ	ω_0	k_l	k_h	β
$L1$	64	665.2	0.5	0.8727	9.139	1.8752			0
$T1$	64	665.2	0.5	0.8727	9.139	1.8752	18	21	0.1
$T2$	64	665.2	0.5	0.8727	9.139	1.8752	18	21	0.5
$T3$	64	665.2	0.5	0.8727	9.139	1.8752	18	21	1.25
$T4$	64	665.2	0.5	0.8727	9.139	1.8752	18	21	2.5
$T5$	128	665.2	0.5	0.8727	9.139	0.4688	30	34	1.
$T6$	128	665.2	0.5	0.8727	9.139	0.4688	30	34	2.5
$T7$	128	2500.							
$T8$	128	a							
$T9$	128	2500							
$T10$	128	a							

[a]See Table I.

coherent structure emerged with bending waves excited and sustained secondary structures winding azimuthally around the vortex. However, in case $T4$ the coherent structure did not survive the interaction with the small scales; that is, after the initial decay of the fluctuations the vortex had disappeared altogether. Based on these four simulations we estimated the parameter values for the high-resolution simulations, $T5$ and $T6$, so as to excite bending waves on the vortex.

The initial random fluctuations of course cannot be characterized as "genuine" turbulence, because they have not adjusted to the presence of the coherent vortex; but this is the only way to introduce well-defined background turbulence field. However, within a few rotations of the vortex the turbulence adjusts to the presence of the coherent structure and thus becomes more realistic. During this time the fine scales decay drastically. That way we obtain a weakly turbulent vortex which we may use as the initial condition for other simulations with increased coherent Reynolds number, because the value of the viscosity is no longer computationally restricted by the fine-scale turbulence but by the coherent vortex. Cases $T9$ and $T10$ (see Tables I and II) are examples of such simulations.

In order to facilitate comparisons with the laminar evolution (case $L1$ in Refs. [12,13]), we designed the turbulent simulations $T1-T6$ (Table I and II) such that the "coherent Reynolds number" Re_c ($=\Gamma/\nu$), based on the coherent vortex, is exactly the same as in case $L1$—the reference laminar case for all turbulent simulations. Thus, the circulation of the vortex was decreased by a factor α whenever the kinematic viscosity was reduced by a factor α.

III. SMALL-SCALE ORGANIZATION

The growth of the incoherent scales is illustrated by considering a plane $\pi_\parallel$ containing the axis of the coherent structure (hence a meridional plane). This structure is initially axisymmetric and would remain so in the absence of the random fluctuations. The coherent vorticity does not initially contribute to ω_n, the vorticity component normal to $\pi_\parallel$, as there is no azimuthal vorticity in the structure at $t=0$. Thus the sizes of regions in $\pi_\parallel$, where the vorticity component ω_n is of one sign, reveal visually the scales associated exclusively with the initial incoherent vorticity; see Fig. 2(a). Subsequently, the coherent structure acquires helical vortex lines and thereby contributes to ω_n. These contributions to ω_n are characterized by the nearly odd symmetry about the axis and have larger scales than the incoherent background; see Figs. 2(b)–2(e). The incoherent scales grow progressively everywhere in the computational domain; see Figs. 2(a)–2(q). This growth cannot be the result of purely diffusive mechanisms because of the absence of intermediate scales at $t=0$. In the following section we show that the organization is the result of an inviscid interaction between coherent structure and the turbulent background.

The growth of incoherent scales in the neighborhood of a coherent vortex, exemplified by case $T5$ in Fig. 2, is typical. Such growth occurs in all turbulent simulations of this type (Tables I and II) and was also seen in our preliminary simulations with initially "white-noise" incoherent vorticity, devoid of any spectral gap. This takes place for all excitation levels of the incoherent vorticity, provided that the underlying coherent vortex survives in some form. However, the effect of the organization on the evolution of the coherent structure itself depends strongly on both the initial excitation level and the coherent Reynolds number as will be shown in a later section.

While Fig. 2, which depicts only the sign of ω_n, shows a growth of incoherent scales, it does not reveal the corresponding vortical structure. For that we need to consider plane sections as well as isovorticity surfaces of $|\omega|$.

TABLE III. Times for frames. (I): Valid for cases $L1$ and $T1-T4$. (II): Valid for cases $T5$ and $T6$.

Frame label	t^* (I)	t^* (II)	t
(a)	0	0	0
(b)	0.5	2.0	5.322
(c)	1.0	4.0	10.644
(d)	1.5	6.0	15.966
(e)	2.0	8.0	21.288
(f)	2.5	10.0	26.610
(g)	3.0	12.0	31.932
(h)	3.5	14.0	37.254
(i)	4.0	16.0	42.576
(j)	4.5	18.0	47.898
(k)	5.0	20.0	53.220
(l)	5.5	22.0	58.542
(m)	6.0	24.0	63.864
(n)	6.5	26.0	69.186
(o)	7.0	28.0	74.508
(p)	7.5	30.0	79.829
(q)	8.0	32.0	85.152
(r)	10.0		106.440
(s)	12.0		127.728

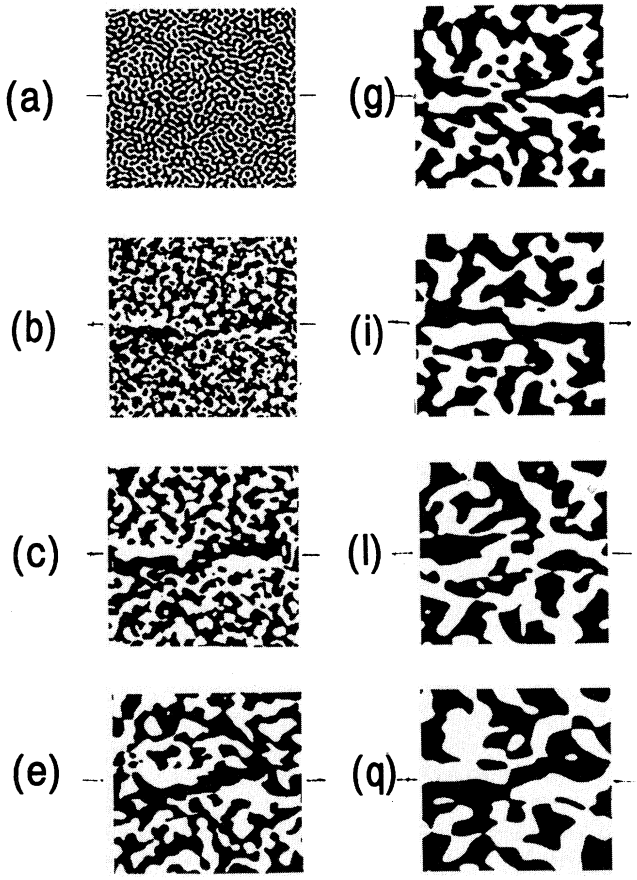

FIG. 2. Positive and negative regions of ω_n in $\pi_{\|}$ for case $T5$ (see Tables I and II). The frame labeling (a), . . . , (q) refers to the times given in Table III; the same labeling is used for same time identification in figures throughout the paper. The horizontal axis of the initially axisymmetric coherent vortex is marked on the side of each frame.

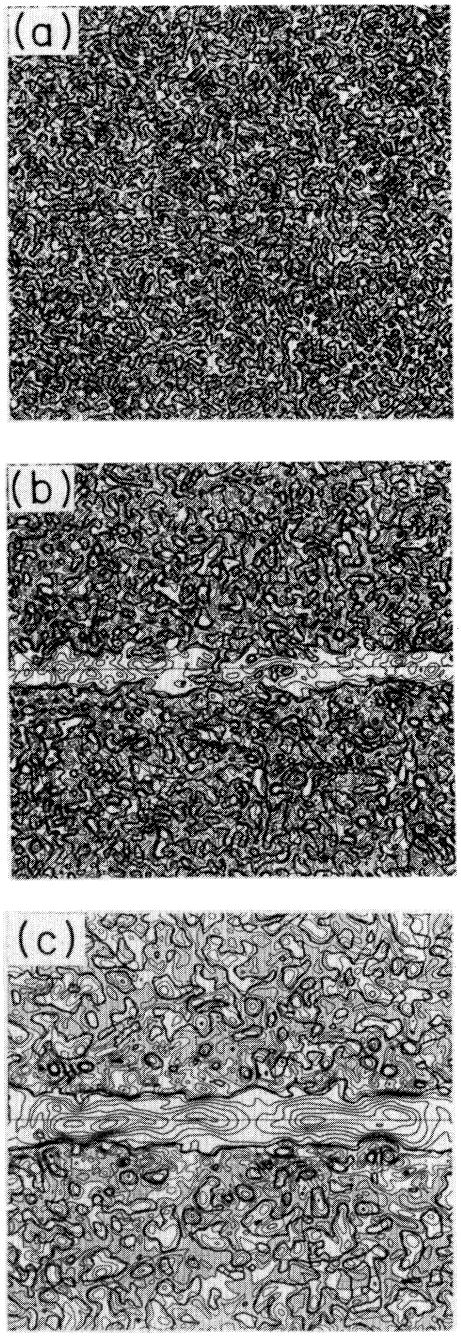

FIG. 3. The vorticity norm in $\pi_{\|}$ for case $T5$ at different times; see Table III. The intersection point of arrows in (g) and (i) indicates the location analyzed later. The contour levels in dimensional units are (a) $\omega_h=70$, $\delta\omega=10$, gray shading for $\omega<10$; (b) $\omega_h=8$, $\delta\omega=1$, gray shading for $\omega<1$, thin contours are for $\omega=0.4,0.8,1.2,1.6$; (c) $\omega_h=4.5$, $\delta\omega=0.5$, gray shading for $\omega<0.4$, thin contours are for $\omega=0.2,0.4,0.8$; (e)–(i) $\omega_h=4.0$, $\delta\omega=0.5$, gray shading for $\omega<0.2$, thin contours are for $\omega=0.05, 0.1, \ldots, 0.45$; (l) $\omega_h=2$, $\delta\omega=0.25$, gray shading for $\omega<0.1$, thin contours are for $\omega=0.02,0.04, \ldots, 0.2$; (q) $\omega_h=1.25$, $\delta\omega=0.25$, gray shading for $\omega<0.1$, thin contours are for $\omega=0.02,0.04, \ldots, 0.2$. For reference the $\mathfrak{W}_k=1$ ($\mathfrak{W}_k\equiv[\omega^2/(2S_{ij}S_{ij})]^{1/2}$ is the kinematic vorticity number) contour is overlaid with a heavy line in each frame.

Figure 3 shows contour levels of $|\omega|$ in $\pi_{\|}$ for the same flow (case $T5$). Initially the incoherent vorticity contributes so much to $|\omega|$ that the coherent structure is indiscernible [Fig. 3(a)]. However, the vorticity magnitude decreases dramatically as a result of viscous decay in the early part of the simulation and as a consequence the coherent vortex quickly becomes discernible; see Figs. 3(b) and 3(c). While the scales of the incoherent vorticity grow every where in the computational domain (Fig. 2), it is only near the coherent structure that the incoherent vorticity magnitude remains appreciable; see Figs. 3(e)–3(q). The fact that the incoherent scale—unlike the vorticity magnitude—appears uniform in the computational domain is a consequence of computational limitations, namely, the size of the coherent structure to the box size. In reality, incoherent vorticity very far away

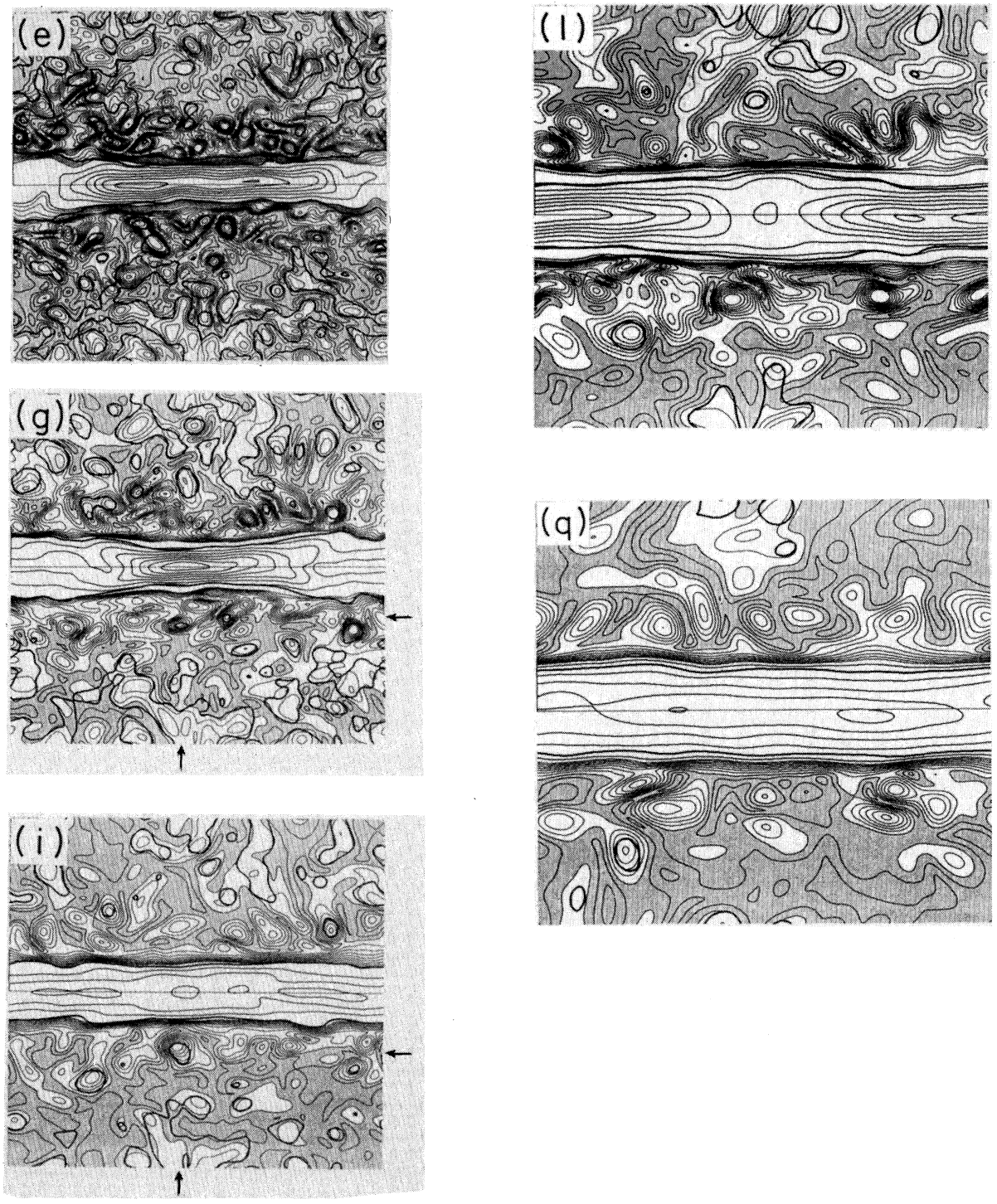

FIG. 3. (*Continued*).

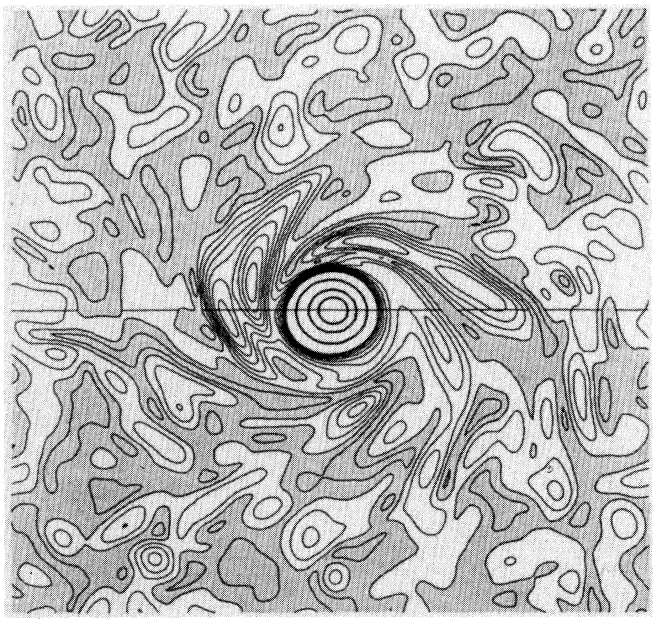

FIG. 4. Cross section of the vortex corresponding to frame (g) of Fig. 3 is shown by the vorticity norm. The lowest contour levels are shaded gray. A smaller contour increment has been used for the low levels than for the high levels.

from the coherent structure will not be influenced by the shear of the vortex and hence will not be subject to organization; however, no part of our computational domain is very far away from the coherent structure.

In a layer surrounding the coherent vortex, we observe interesting vortical dynamics, reminiscent of 2D turbulence; see Figs. 3(e)–3(q). This dynamics is driven by the shear induced by the coherent structure, for the small vortical structures are being wound around it in a spiral fashion. Figure 4 which shows a cross section perpendicular to the axis of the vortex at a z location indicated by the upward arrow in Fig. 3(g). A 3D isovorticity plot, Fig. 5, reveals that incoherent vortical structures are swirling azimuthally around the coherent structure. We recognize similarities with the growth of the boundary layer on an impulsively rotated rod [14,15]. However,

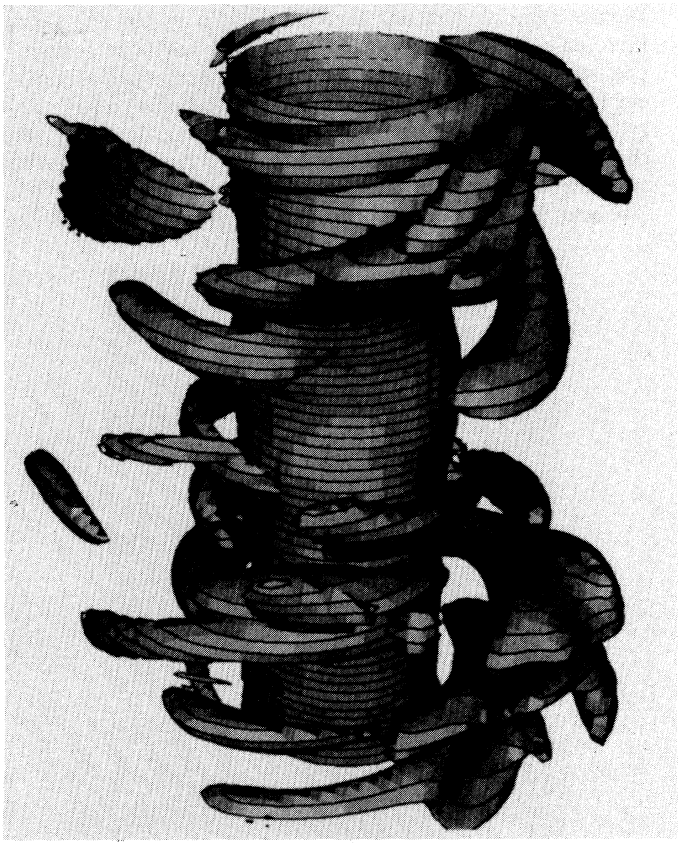

FIG. 5. Isovorticity surface for case $T5$ corresponding to frame (q) of Fig. 3. The vorticity norm on the surface equals 10% of the peak value.

there is an important difference in that the spiral structure in our case features an obvious lack of axisymmetry (Fig. 4).

IV. VISCOUS AND INVISCID ASPECTS OF THE SMALL-SCALE ORGANIZATION

The small-scale organization starts with the azimuthal alignment of the random vorticity in a layer surrounding

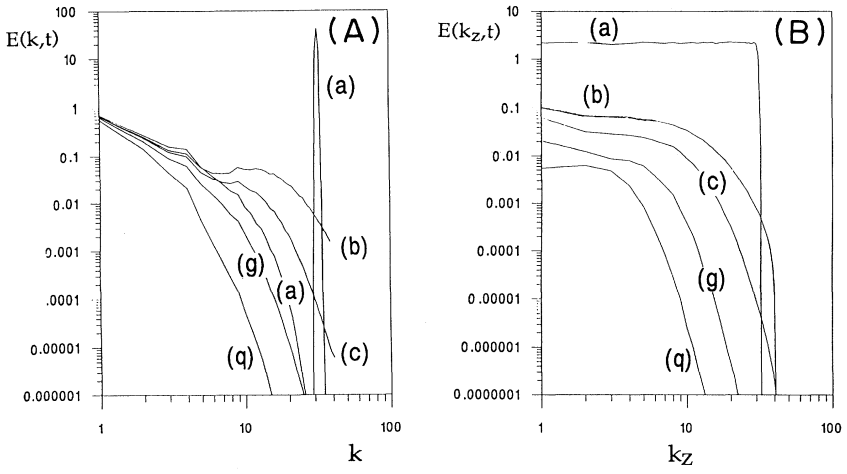

FIG. 6. (A) Energy spectrum $E(|\mathbf{k}|,t)$ for case $T5$ corresponding to frames (a), (b), (c), (g), and (q) of Fig. 3. (B) Energy spectrum $E(k_z,t)$ corresponding to frames (a), (b), (c), (g), and (q) of Fig. 3.

the vortex; see Fig. 4. This alignment is obviously an inviscid phenomenon for it is driven by the shear induced by the coherent vortex. Once the vorticity in the surrounding layer through the alignment acquires a preferred direction (roughly parallel to the azimuthal direction) the dynamics become subject to the similar geometrical constraints as 2D vorticity dynamics. Therefore pairing of small-scale structures must be considered as a possible inviscid mechanism for the organization. We must carefully distinguish between this inviscid mechanism and simple viscous decay which also produces a growing scale.

The energy spectrum $E(|\mathbf{k}|,t)$ for case $T5$ is shown in Fig. 6(A). The initial spectral gap which is clearly evident at $t^*=0$ has disappeared at $t^*=0.5$ due to the strong damping. Most of the energy in the initial small-scale peak cascades to higher wave numbers where it is dissipated. Some energy is, however, transferred to smaller wave numbers early on (before $t^*=0.5$) as seen by comparing the spectra at $t^*=0$ and $t^*=0.5$. If the small-scale peak in the spectrum had been a steady forcing this would result in a k^4 infrared spectrum (Lesieur [16], p. 194). Such an infrared spectrum does not develop here because the peak quickly disappears by decay. The strong decay is evident at later times through the rapid tailing off of the spectrum and its growing scale. The energy associated with the coherent vortex is mainly in the axial wave number (k_z) equal to zero, therefore the small scales in the surrounding layer are more clearly diagnosed by the spectrum $E(k_z,t)$; see Fig. 6(B). This spectrum builds up a k^{-12} tail. The energy transfer spectrum (Fig. 7) shows a growing scale and that the energy is

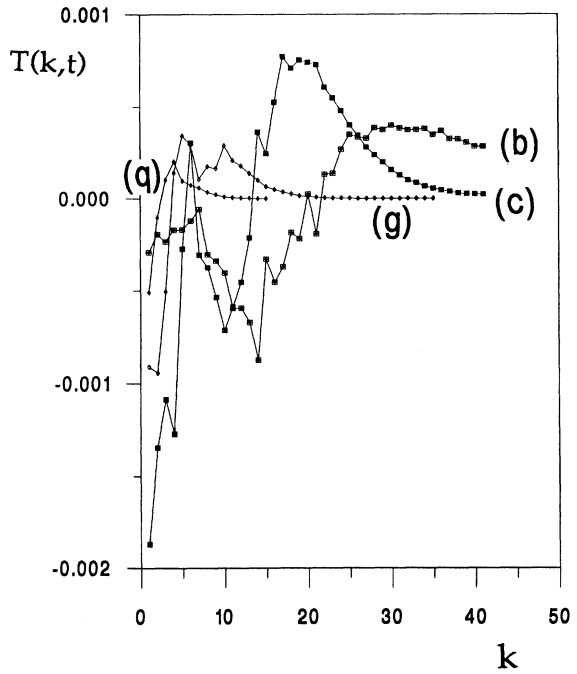

FIG. 7. Energy transfer spectrum $T(|\mathbf{k}|,t)$ for case $T5$ corresponding to frames (b), (c), (g), and (q) of Fig. 3. Note that the curve labeled (b) has been scaled by 0.1.

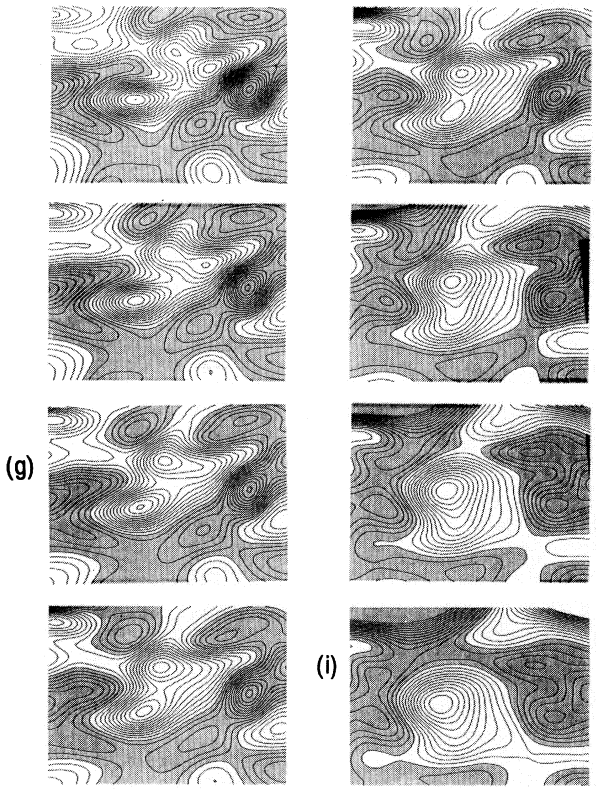

FIG. 8. Enlarged view of a pairing event occurring in simulation $T5$, illustrated by contours of ω_n in $\pi_{\|}$, with negative values shown by gray shading. The enlarged area contains the two small-scale vortical structures indicated by arrows in Fig. 3(g). The successive frames (top to bottom) are at $t^*=2.75$, 2.875, 3.0, 3.125, 3.25, 3.5, 3.75, 4.0.

transferred from larger to smaller scales. Thus the coherent vortex cascades energy to the smaller scales in the surrounding layer through vortex stretching. We emphasize that the possible occurrence of pairings is not ruled out by this type of energy transfer and that pairings do not imply a net inverse energy cascade.

By following the evolution of individual small scale structures in the surrounding layer we find events that closely resemble pairings. That is, structures of the same polarization (see Sec. V) combine into larger ones when they come in close proximity. An example is given in Fig. 8 which shows in an expanded view the details of the amalgamation of the two structures identified by two arrows in Fig. 3(g); these structures have combined into the similarly identified structure in Fig. 3(i). If this is indeed a pairing event, then it is of course very viscous and lacks the fine-scale filaments seen in 2D simulations at much higher Reynolds numbers [17]. Moreover, in Fig. 8, the cross section is in a fixed plane in space, while the small structures are actually swirling around the coherent structure. This swirling is the reason for the outward displacement (downward shift of the vorticity peak in Fig. 8) of the paired small scale structure; compare Figs. 8(g) and 8(i). The motion of the small structures normal to the

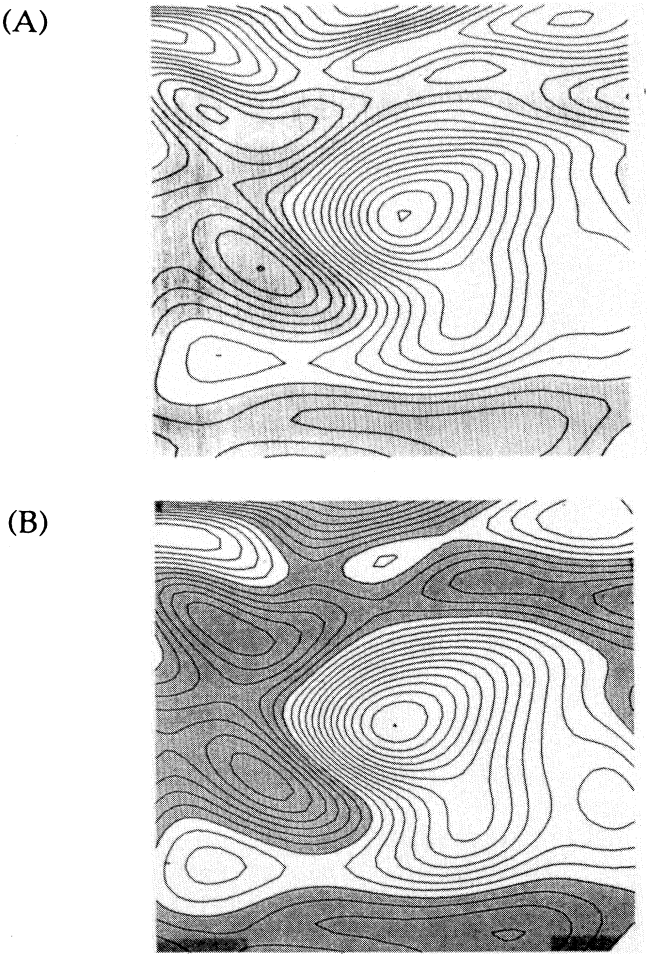

FIG. 9. End result of simulations $T7$ (A) and $T8$ (B), both of which have the flow field in Fig. 3(g) as the starting conditions. The cross sections should be compared with frame (i) of Fig. 8.

cross-section plane also makes the pairing event appear slower than it in fact is.

In order to see whether the sequence of events captured and magnified in Fig. 8 is a pairing, and hence, an inviscid phenomenon smoothed out by diffusion or just a consequence of the viscous decay and a growing scale in the background, we restarted the calculation from Fig. 3(g) with reduced damping, i.e., cases $T7$ and $T8$. In case of $T7$ the Reynolds number is increased by a factor of 4, while in case $T8$ the artificial viscosity $\nu_4\Delta^2$ (so-called hyperviscosity) is applied. The latter reduces the energy decay drastically as only the very smallest scales are subjected to significant damping. In both cases the pairing event occurs within the same time in spite of the different and smaller damping; see Figs. 9(A) and 9(B). Thus the event captured in Fig. 8 is an inviscid pairing, which will occur at all Reynolds numbers and which can only be smoothed by viscous effects. We conclude that the small-scale organization is an inviscid phenomenon with pairing being the central mechanism.

Even though axial transport is slow relative to the swirl velocity it is of central importance. For axial transport can bring distant small-scale structures in close proximity—thus enabling them to pair. There are three axial transpot phenomena: dipole motion of nearby threads with opposite signed azimuthal vorticity, curvature induced motion of individual threads, and advection in the meridional flow of the coherent vortex.

In addition to the inviscid pairing mechanism for the production of larger structures, there are also inviscid mechanisms generating new smaller scales in the surrounding layer. Filamentation from the thread cores is one such mechanism. Another is that a thread can peel vorticity out of the coherent vortex. Moreover, the coherent vortex can itself shed vorticity into the surrounding layer. Finally, vortex stretching by the coherent vortex can also produce small scales by shrinking the thread cores.

V. THE NATURE OF THE INTERNAL INTERMITTENCY NEAR A COHERENT STRUCTURE

The spiral structures surrounding the coherent structure (Fig. 5) constitutes a new type of internal intermittency. We find mainly axial vorticity inside the vortex and mainly azimuthal vorticity in the surrounding layer. Note that the spiral structures are threadlike rather than sheetlike. These threads have high helicity and are highly polarized in the sense of the generalized Helmholtz decomposition [16]—a point that we elaborate on in the following.

The generalized Helmholtz decomposition splits a 3D vector field into three rotationally invariant parts: a potential part, a left- and a right-polarized part. The sum of the latter two yields the rotational part of the field. Locally the vector lines of the left (right) polarized part form left-handed (right-handed) helixes, hence their names. The decomposition is accomplished by using the complex helical-wave decomposition [13,16]. The decomposition reveals an important feature of the spiral threads surrounding the coherent vortex, namely, individual structures are either predominantly right handed or predominantly left handed. Figure 10 gives an overall picture of this phenomenon by showing surfaces of constant $|\omega_R|$ [Fig. 10(A)] and $|\omega_L|$ [Fig. 10(B)] at the end of simulation $T5$. When these surfaces are overlaid [Fig. 10(C)] we see that the polarized components tend to occupy separate locations in the surrounding layer. This is a clear indication of small-scale polarization and spatial separation of the peak regions of right- and left-handed polarized components.

In order to quantitatively assess the degree of the small-scale-structure polarization we must make a pointwise comparison of the amplitudes of the polarized vorticity components ω_R and ω_L. For that purpose we introduce the quantity

$$\mathcal{R}(x,y,z)\equiv\log_2[\,|\omega_R(x,y,z)|/|\omega_L(x,y,z)|\,]\ . \qquad (2)$$

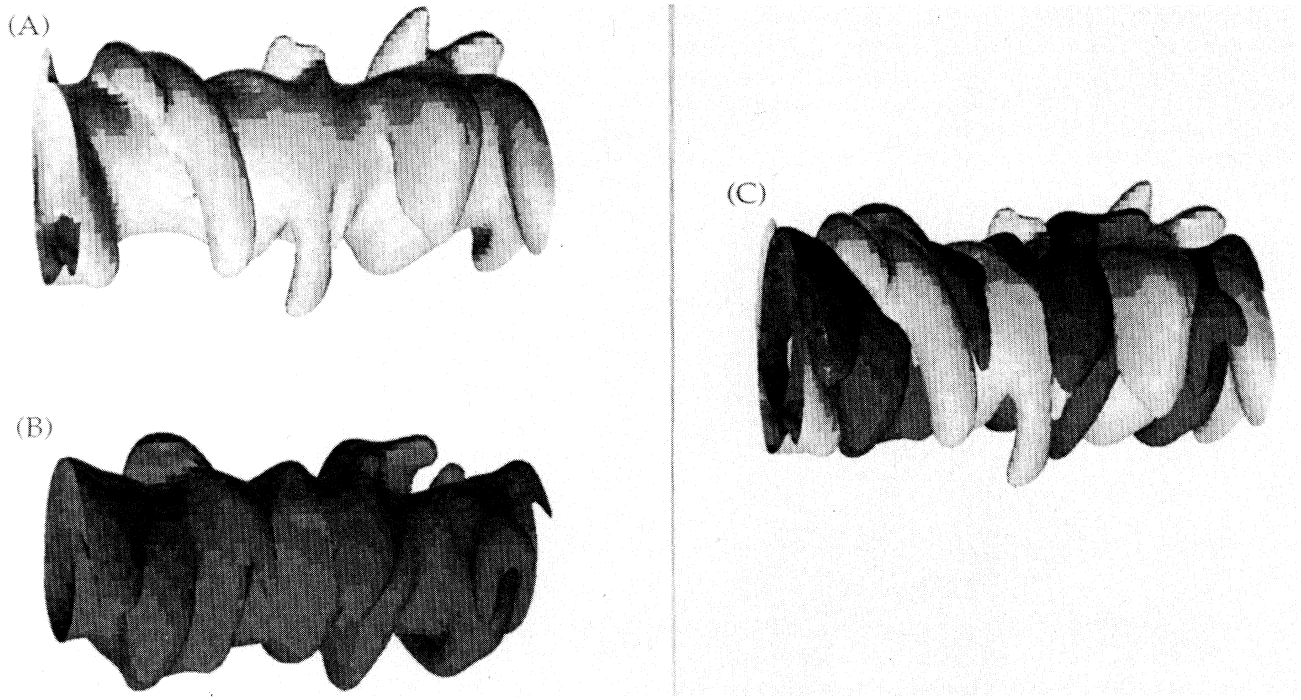

FIG. 10. Isovorticity surfaces of the polarized vorticity components corresponding to frame (q) of Fig. 3. The light-shaded surface is the right-handed contribution (A), the dark-shaded surface is the left-handed one (B). The overlay of the two is shown in (C).

$\mathcal{R}$ equals zero when there is a balance between left and right components (i.e., no polarization); $\mathcal{R}$ is positive when the right component dominates and negative when the left dominates. The absolute value of $\mathcal{R}$ gives a measure for the degree of local polarization. A logarithmic function is used in (2) because $\mathcal{R}$ shows large spatial variations. For convenience we use the logarithmic function with base 2. Figure 11 shows the contours of $\mathcal{R}$ for case $T5$. Already the initial conditions exhibit significant polarization in the random small scales, in that $\mathcal{R}$ ranges from approximately -5 to 5, [Fig. 11(a)]. This range of $\mathcal{R}$ changes only little through the evolution. Figure 11 clearly shows that the small-scale organization is accompanied by a similar organization in the left and right handedness of the vorticity field, which can hardly be surprising as the characteristic scale in the turbulent background grows continuously through the evolution. The central issue that we must address is whether local peaks of $|\mathcal{R}|$ are associated with local peaks of $|\boldsymbol{\omega}|$ (i.e., small-scale structures) in the surrounding layer. Thus we must compare corresponding frames of Figs. 3 and 11.

This comparison is nontrivial, for $\mathcal{R}$ is not conditioned with respect to vorticity magnitudes. That is, $|\boldsymbol{\omega}_R|$ and $|\boldsymbol{\omega}_L|$ may both be very small at a given point, in which case the value of $\mathcal{R}$ is not of any interest. Note that $|\boldsymbol{\omega}_R|=0 \wedge |\boldsymbol{\omega}_L|=0$ implies $|\boldsymbol{\omega}|=0$, but $|\boldsymbol{\omega}|=0$ does not imply $|\boldsymbol{\omega}_R|=0 \wedge |\boldsymbol{\omega}_L|=0$. Note that subscripts R and L denote right- and left-handed components. Hence the best way to discount irrelevant peak in $\mathcal{R}$ is, for a given peak in Fig. 3, to search for a corresponding peak in Fig. 11. Using this procedure, we readily find a significant degree of polarization (i.e., $|\mathcal{R}|>1$) for most small structures in the surrounding layer. For example, in frame (q) there are about 17 significant peaks of $|\boldsymbol{\omega}|$ in the surrounding layer [Fig. 3(q)]—15 are matched closely by peaks of $\mathcal{R}$ [Fig. 11(q)]. Note that in general there is a small distance between corresponding peaks in Figs. 3 and 11, but the correlation is clear. We notice that in frame (q) as well as in other frames there are a only a few (less than 10%) small-scale structures in the surrounding layer which show little polarization ($|\mathcal{R}|<0.5$). Outside the surrounding layer, however, the correlation between polarization peaks and small-scale vortical structures deteriorates with the distance from the coherent structure.

The small-scale structures surrounding the coherent vortex are aligned with or against the swirl: the right-handed structures are aligned with the swirl and the left-handed ones are aligned against it, as indicated in Fig. 12(A). We can obtain a rough understanding of this phenomenon by considering the vector lines of $\boldsymbol{\omega}_R$ and $\boldsymbol{\omega}_L$ near the coherent vortex (note that these lines should not be confused with the regular vortex lines, which are the vector lines of $\boldsymbol{\omega}$). Both $\boldsymbol{\omega}_R$ and $\boldsymbol{\omega}_L$ have a positive mean z component inside the coherent vortex. Since, furthermore, the $\boldsymbol{\omega}_R$ lines are locally right-handed helixes we can roughly expect an $\boldsymbol{\omega}_R$ line, which enters or exits the coherent vortex core, to have a positive ω_θ component as sketched in Fig. 12(B). When a similar argument is applied to the $\boldsymbol{\omega}_L$ lines, which are left-handed helixes, we find that they have negative ω_θ in the surrounding layer [Fig. 12(C)]. Hence we can roughly expect that

$$\boldsymbol{\omega}_R \cdot \mathbf{e}_\theta > 0 \wedge \boldsymbol{\omega}_L \cdot \mathbf{e}_\theta < 0 \tag{3}$$

in the surrounding layer; here $\mathbf{e}_\theta$ is a unit vector in the azimuthal direction. Figures 12(D) and 12(E) show that the above argument has merit, but also show that it is not always true. At a distance away from the coherent vortex the argument fails completely, which can hardly be surprising given the turbulent nature of the flow. More significantly, the argument occasionally also fails within the surrounding layer, because of phenomena as illustrated in Fig. 12(F).

Some of the phenomena described above may also be inferred from the helicity density [Fig. 12(G)] with the present choice of inertial frame (i.e., no translational ve-

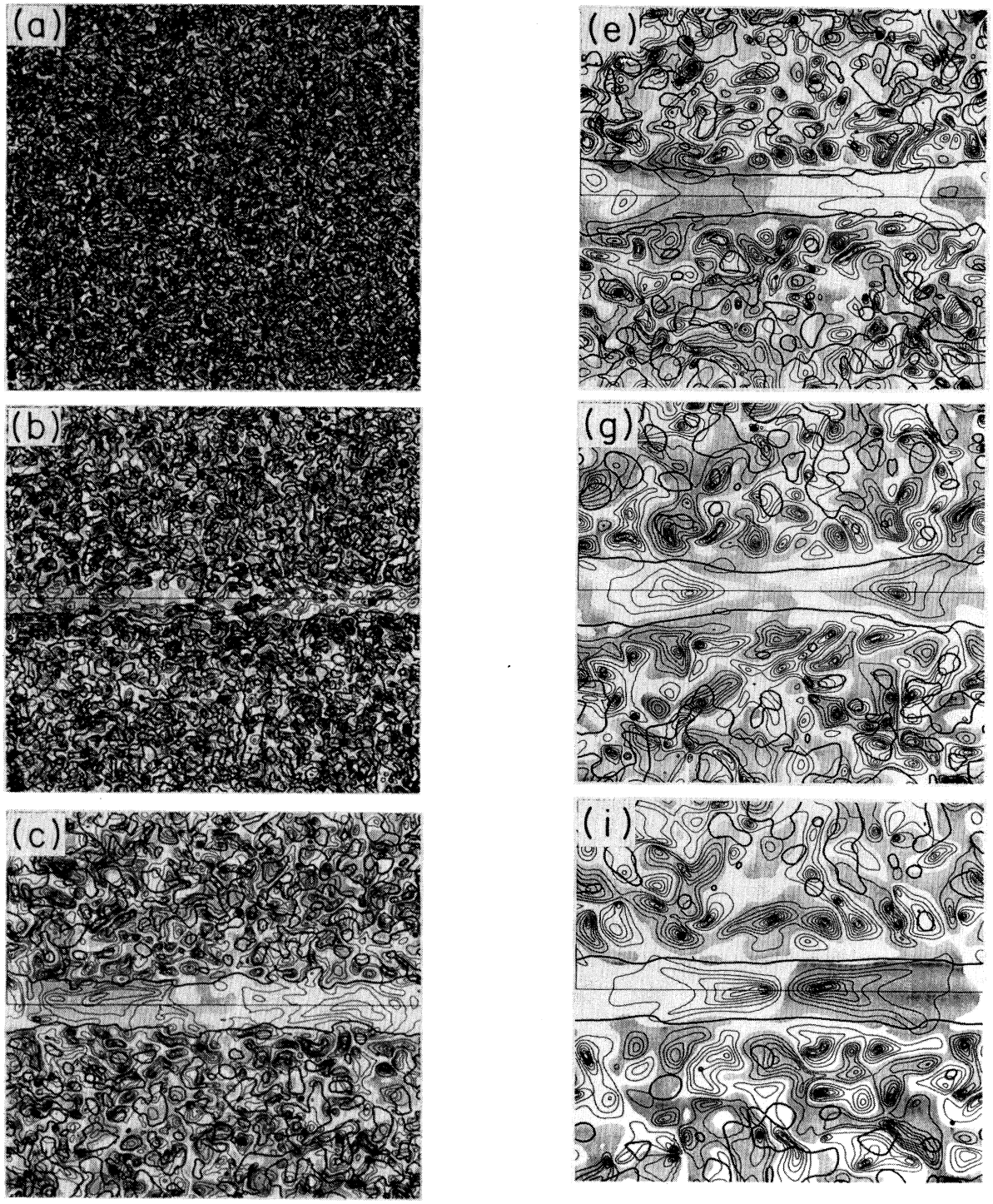

FIG. 11. Pointwise polarization ratio $\mathcal{R}$ [defined in Eq. (2)] for case $T5$ is shown in plane $\pi_\parallel$ at times given in Table III. Contour levels are in increments of 0.5 and the negative values are marked by gray shading. For reference the $\mathfrak{W}_k = 1$ contour is overlaid with a heavy line in each frame.

locity at infinity). This is due to the dominance of the azimuthal vorticity and velocity components in the surrounding layer. However, we emphasize that the helicity density is no substitute for the helical decomposition. There are a number of reasons for this. First, the helicity density is not a local characterization of the vortex lines but of the streamlines. Second, it is not possible to express the Navier-Stokes equations in terms of the helicity density. Third, the helicity density only shows the alignment of vorticity and velocity in the surrounding layer and hence picks out the spirally aligned small-scale structures, but the local polarization of these small scales cannot be inferred.

Figure 13 shows the dissipation contours in $\pi_{\|}$. Comparison of Figs. 11 and 13 does not reveal any correspondence between high values of $\mathcal{R}$ and low values of the dissipation. Neither does one observe a consistent correspondence between low dissipation and high values of the helicity density [compare Fig. 12(G) and Fig. 13(g)]. In fact there are examples of local helicity peaks coinciding with local peaks in the dissipation. Hence, we cannot draw any conclusions regarding spatial regions of high or low dissipation, polarization, and helicity.

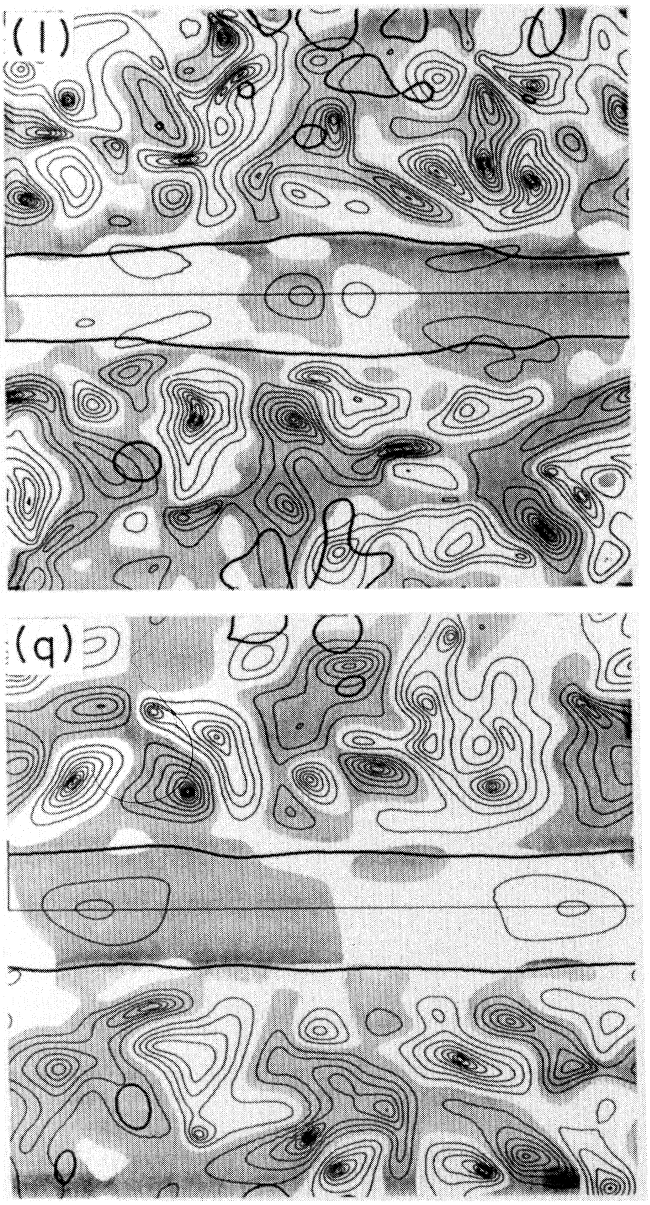

FIG. 11. (*Continued*).

VI. POLARIZATION MECHANISMS INHERENT IN THE SMALL-SCALE ORGANIZATION

There are interesting consequences of the shear-induced alignment resulting from the presence of the coherent vortex. The foremost effect is to provide the vorticity in the surrounding layer with a preferred direction (roughly the azimuthal direction) and thus enable the well-known dynamics of 2D vortices (pairing or merger, dipole motion, and axisymmetrization), albeit in a modified form. We now focus our attention on how this quasi-2D vortex dynamics makes the small-scale structures highly polarized.

It is essential to notice that the vorticity after the initial alignment is not exactly aligned with the azimuthal direction, but have vortex lines showing spiral pattern as sketched in Fig. 14(A); see also the cross section in Fig. 4 [which corresponds to frame (g)]. The spiral pattern is not stationary as the angle ϕ with the azimuthal direction decreases with time. This is because the azimuthal velocity induced by the coherent vortex increases as one moves towards the vortex along one of the spiral arcs shown in Fig. 14(A). The coherent shear and hence vortex stretching of the spirally aligned small-scale structures also increase along the arc (as can be inferred from r^{-1} induction velocity variation outside the coherent vortex). As a result, the vorticity magnitude increases along the spiral arc. It follows that there is a differential rotation along a small-scale structure in the surrounding layer; see Fig. 14(B). This differential rotation gives the structure an intrinsic tendency to become polarized. As illustrated in Fig. 14(B), structures with vorticity pointing in the direction of the coherent vortex's swirl become predominantly right handed while structure with vorticity pointing against the swirl becomes predominantly left handed. We call this phenomenon *internal polarization* of the small-scale structures.

Another important aspect of the spiral geometry shown in Fig. 14(A) is that the distance between two neighboring spiral arcs increases with increasing radius (see also Fig. 4). When two small-scale structures pair in the surrounding layer as shown in Fig. 14(C), then an obvious consequence of the spiral geometry is that the pairing takes place faster close to the vortex than away from it. Thereby the vortex lines acquire additional coiling and hence stronger polarization as shown schematically in Fig. 14(C). Thus pairings of the small scales with the same polarization maintain and may even enhance the small-scale polarization.

There is another mechanism that follows from the spiral geometry shown in Fig. 14(A). Consider a small-scale structure surrounded by weak vorticity without any preferred polarization [Fig. 14(D)]. Clearly the weak vor-

ticity will be wrapped around the small-scale structure; in addition, it will be advected by the swirl induced by the coherent vortex. Because of the fact that the spin velocity increases as one approaches the coherent structure along the spiral arc (on which a secondary structure lies) shown in Fig. 14(A) it follows that the weak vorticity becomes polarized. In fact, the weak vorticity acquires the same polarization as the small-scale structure around which it wraps. These, therefore, are some of the mechanisms for small-scale organization in turbulent shear flows.

VII. EFFECT OF THE SMALL-SCALE ORGANIZATION ON THE DYNAMICS OF THE COHERENT STRUCTURE

The simulations $T1-T6$ are all decaying flows as no energy is supplied to replenish dissipative losses. Consequently, these unforced flows will eventually laminarize. The time scale at which this happens depends both on the Reynolds number Re_c (based on the coherent vortex) as well as on the initial turbulent fluctuation level (say, the Reynolds number based on the Taylor microscale for the initial turbulent background flow). Depending on the ini-

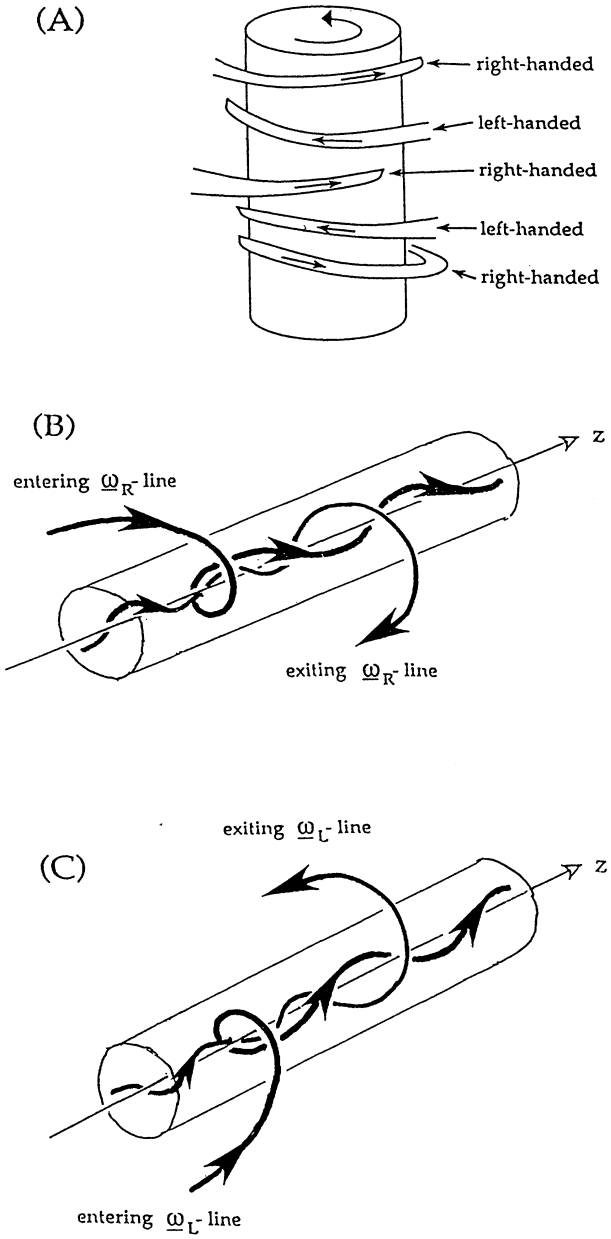

FIG. 12. (A) Sketch of the general orientation of the left- and right-handed small-scale vortical structures surrounding the coherent vortex. (B) Sketch of the right-handed vorticity components vector lines. (C) Sketch of the left-handed vorticity components vector lines. (D) Contours of normal component of ω_R in $\pi_{\|}$. (E) Contours of normal component of ω_L in $\pi_{\|}$. (F) Highly localized coiling of vector lines. (G) Contours of the helicity density $h=\mathbf{u}\cdot\boldsymbol{\omega}$ in $\pi_{\|}$.

tial turbulent fluctuation level one of three things happens. (1) For low random fluctuation levels, the coherent vortex recovers its axisymmetry completely, and although secondary structures do exist in the surrounding layer, their vorticity amplitude keeps decreasing relative to that of the vortex. In such cases, the coherent vortex quickly ceases to be turbulent. (2) For sufficiently high fluctuation levels, the vortex is unable to survive the turbulent environment and is completely disrupted. No sign remains of a coherent vortex of any sort after the initial decay of the turbulent background. However, the quality of the early part of the simulation is questionable for such simulations, as the spectrum tends to lift up too much at the high wave numbers for the simulation to be adequately resolved. Thus, in such cases, we have at best a crude large eddy simulation at early times. (3) For fluctuation levels in between, a vortex survives in some coherent form and the turbulence is sustained for some period of time in the surrounding layer.

Bending waves can be excited if the initial fluctuation level is sufficiently high. In fact, the difference between cases $T5$ and $T6$ is the excitation of bending waves in the latter. The presence of these bending waves also has an influence on the turbulence sustaining mechanism around the vortex. As small-scale vortical structures become more and more azimuthally aligned around the vortex, their radial vorticity component diminishes and vortex stretching diminishes (e.g., for concentric vortex ring around a line vortex there is no stretching). The bending waves alter this by making the stretching more non-

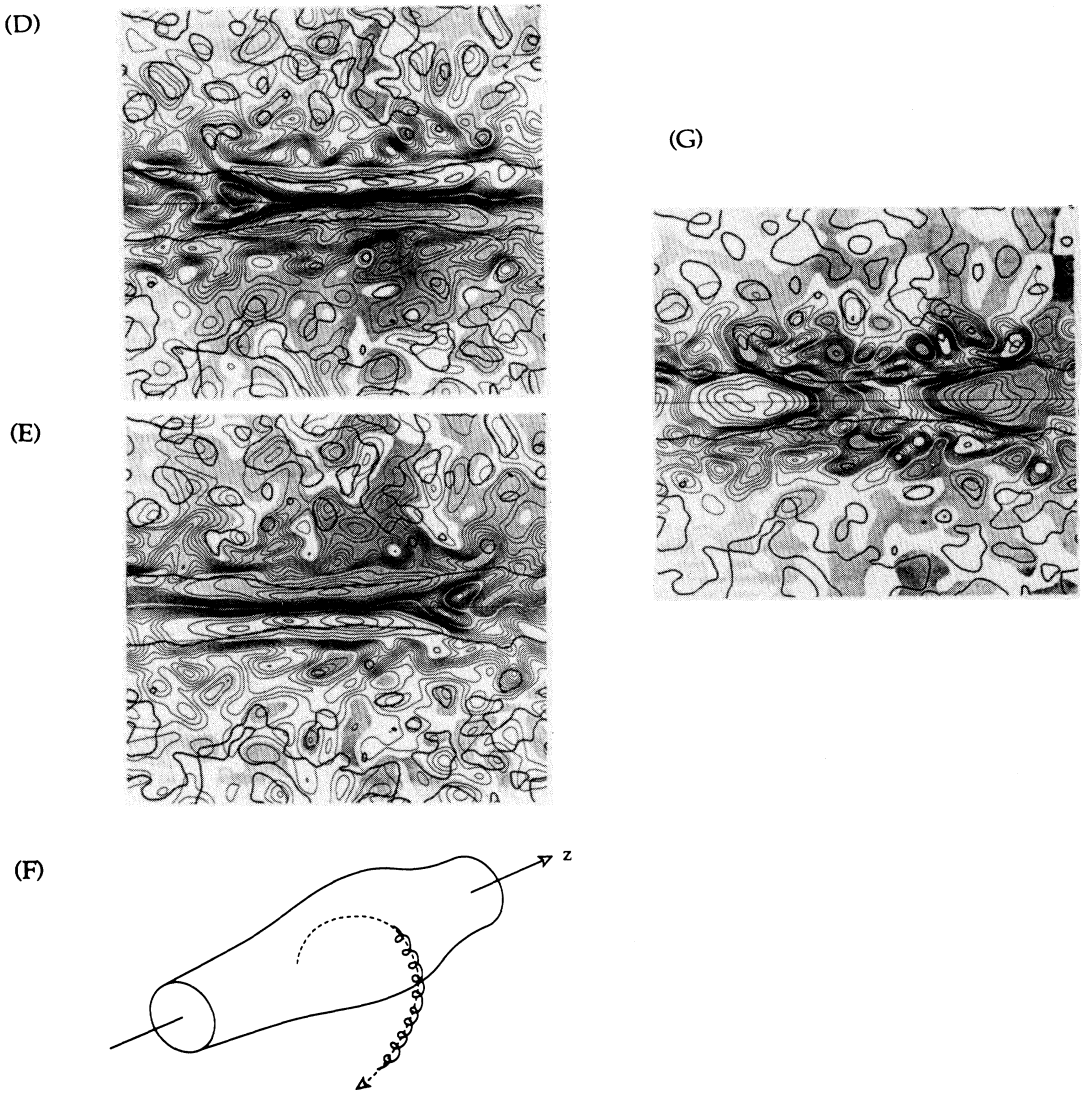

FIG. 12. (*Continued*).

axisymmetric.

Simulations $T9$ and $T10$ start up from the end result of case $T5$ as the initial condition but with reduced damping. In the case of $T9$, the Reynolds number is higher and in $T10$ a small artificial viscosity is employed (see Tables I and II for numerical values). Hence the initial condition for these simulations is a slightly turbulent vortex. The drastically reduced damping allows the small-scale vortical structures in the surrounding layer to become more energetic. This is because these structures obtain their energy from the coherent vortex through an

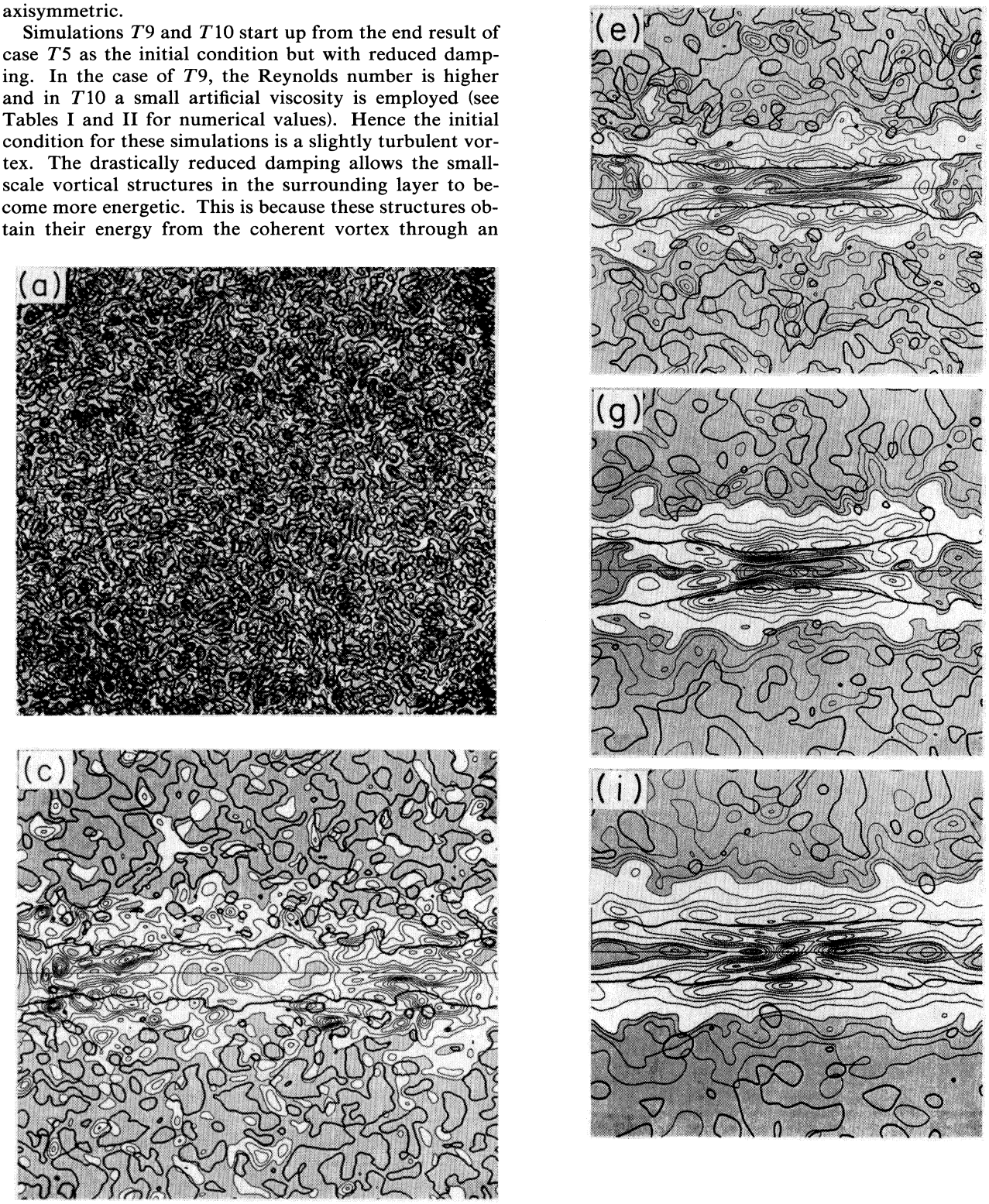

FIG. 13. Contours of dissipation in the plane $\pi_{\|}$ for case $T5$ at times given in Table III. The contour levels are in dimensional units: (a) $\epsilon_h=3000$, $\delta\epsilon=300$, gray shading for $\epsilon<600$; (c) $\epsilon_h=3.6$, $\delta\epsilon=0.4$, gray shading for $\epsilon<0.4$; (e) $\epsilon_h=2.0$, $\delta\epsilon=0.2$, gray shading for $\epsilon<0.4$, thin contours are $\epsilon=0.05,\ 0.1,\ldots,0.35$; (g) $\epsilon_h=1.6$, $\delta\epsilon=0.16$, gray shading for $e<0.32$, thin contours are $\epsilon=0.04,0.08,0.28$; (i) $\epsilon_h=0.81$, $\delta\epsilon=0.09$, gray shading for $\epsilon<0.18$; (l) $\epsilon_h=0.4$, $\delta\epsilon=0.04$, gray shading for $\epsilon<0.04$, thin contours are $\epsilon=0.01,0.02,\ldots,0.08$; (q) $\epsilon_h=0.16$, $\delta\epsilon=0.016$, gray shading for $\epsilon<0.032$, thin contours are $\epsilon=0.004,0.008,0.012$. For reference the $\mathfrak{W}_k=1$ contour is overlaid with a heavy line in each frame.

inviscid cascade mechanism (i.e., stretching) and lose energy mainly by viscous damping, which is now strongly reduced compared to case $T5$. This phenomenon is clearly revealed by the energy transfer spectrum [Fig. 15(A)] and the corresponding energy spectrum [Fig. 15(B)]; both spectra are plotted for the end of simulations $T9$ and $T10$, whose durations are 50% of the duration of $T5$. Moreover, the small-scale structures gain enstrophy and the peak vorticity magnitude in the surrounding layer increases [Figs. 16(A) and 16(B)]. Consequently, the vortex becomes turbulent again. This has implications for the generation of bending waves, which can be excited by energetic small-scale structures. By comparing isovorticity surfaces at the end of simulations $T9$, $T10$ [Figs. 17(A) and 17(B)] with the initial condition [Fig. 17(C)], we observe that the small scales have made the vortex nonaxisymmetric through the excitation of bending waves.

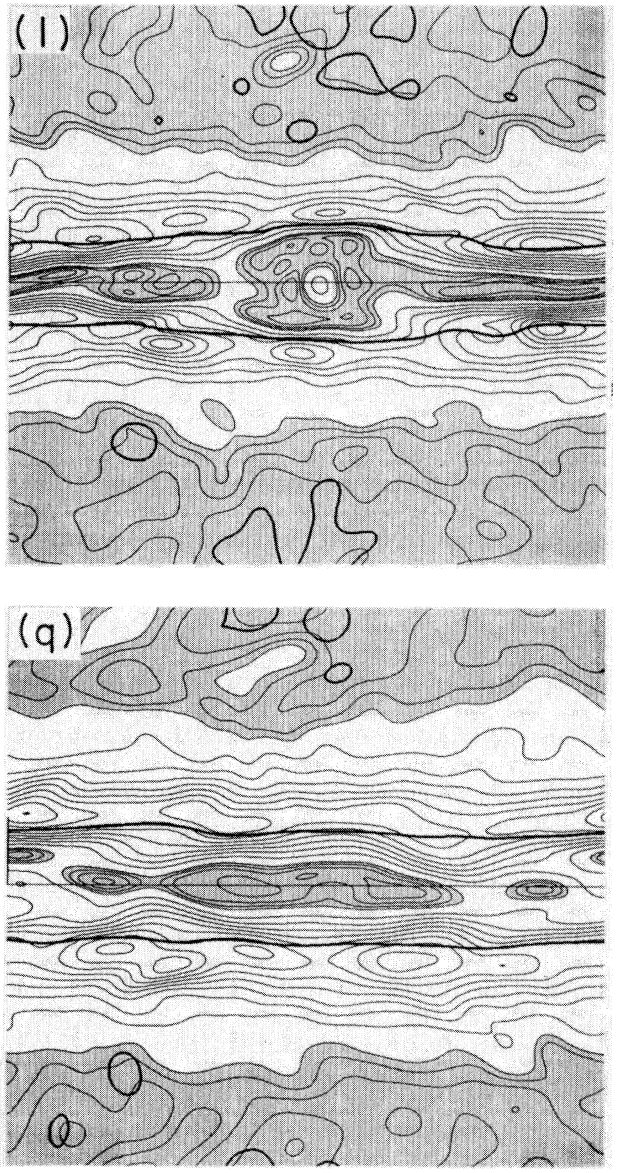

FIG. 13. (*Continued*).

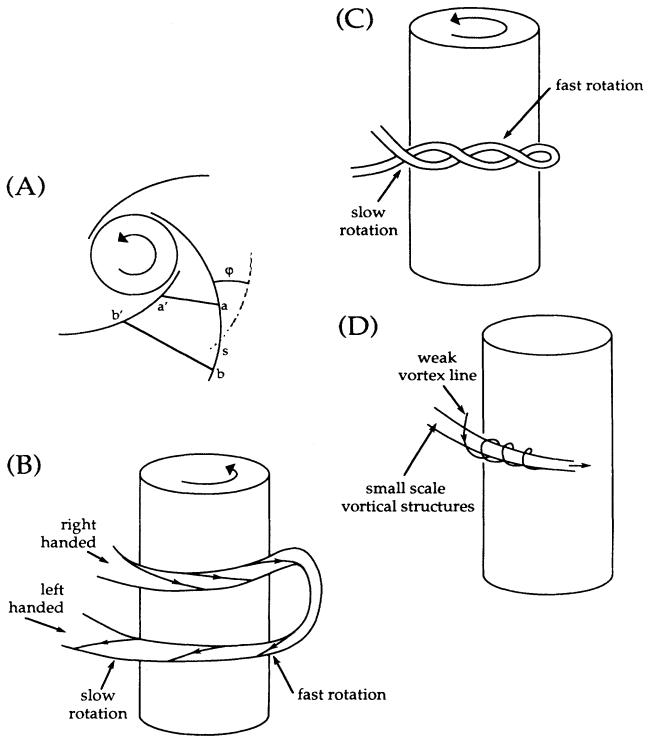

FIG. 14. (a) Schematic of the spiral vortical structure surrounding the coherent vortex. (b) The differential rotation which causes the polarization of the small-scale vortical structures. (c) Increase and maintenance of polarization during pairing events in the surrounding layer. (d) Polarization of weak vorticity surrounding a small vortical structure.

This phenomenon is the sole result of feedback (or backscatter) from the small scale on the coherent vortex, a process which cannot be modeled by enhanced diffusivities. For example, it would not be possible to predict where the bending waves would develop.

Apart from the bending waves the main effect of the turbulence on the coherent vortex dynamics is to slow the motion of the helical-wave packet (discussed later). For case $T5$, one observes core dynamics which except for a slower evolution closely resemble that of case $L1$. At the end of simulation $T5$, the small scales in the surrounding layer have lost their energy and the coherent vortex is largely axisymmetric and rectilinear; see Fig. 3(q).

The quantity $\mathcal{R}$ is useful as a measure of the intensity of the internal core dynamics within the coherent structure. That is, high amplitudes of $\mathcal{R}$ within the core signals strong core dynamics. This is because the core dynamics is driven by differences between the left- and right-handed vorticity components [13]. In Fig. 11, $\mathcal{R}$ thus reveals the motion of helically polarized packets within the core. The large-scale motion inside the vortex core immediately breaks the random distribution in Fig. 11(a) by making the contracting part of the vortex left handed and the expanding part right handed; see Fig. 11(c). The motion of the helical-wave packets on the vortex makes $\mathcal{R}$ significantly more coherent inside the vortex than outside; see Figs. 11(b)–11(e). The low enstrophy

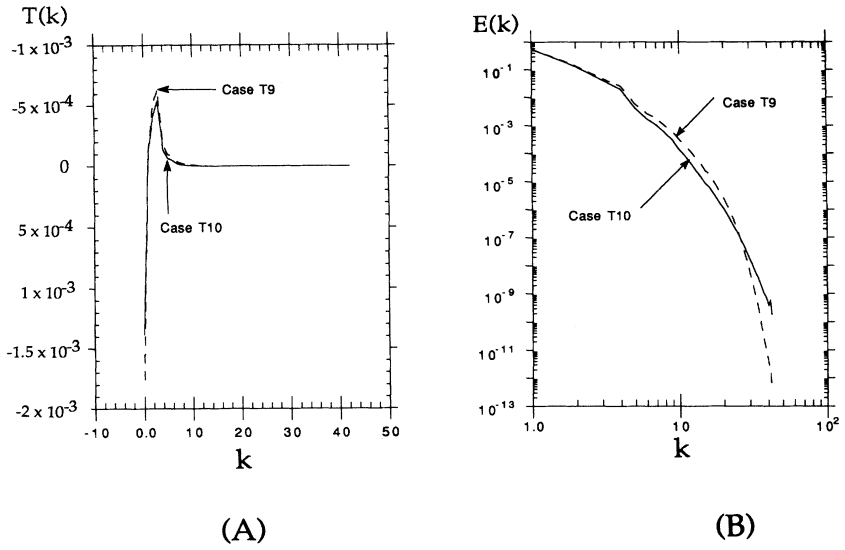

FIG. 15. (A) Energy transfer spectra at the end of simulations $T9$ and $T10$. (B) Corresponding energy spectra.

"bubble" which formed in each of the polarized vorticity components for the laminar case $L1$ (see Refs. [12,13]) also forms in the turbulent case; see Figs. 11(g) and 11(i). Note that the sharp peaks inside the vortex core [Figs. 11(g) and 11(i)] are the result of these bubbles; for example the bubble in the ω_L distribution gives a positive peak in $\mathcal{R}$ as $|\omega_L| \ll |\omega_R|$. The bubbles in the polarized vorticity components coalesce in Fig. 11(l) (or shortly before), thereby producing a bubble in the ω field [Fig. 3(l)]. Compared to the laminar case $L1$ this event occurs significantly later in the turbulent case $T5$. The reason for this delay is that the small-scale turbulence enhances dissipation and diffusion and thus reduces the mean vorticity inside the vortex core faster than in the laminar case. As the core dynamics otherwise are qualitatively similar to the laminar case, this delay in the evolution could be modeled by an eddy viscosity. However, other aspects of the evolution such as the small-scale polarization cannot be modeled this way. As for the laminar simulations [13], the polarized vorticity components enable us to analyze the dynamics within the coherent structure in terms of wave packets moving in opposite directions along the axis of the coherent vortex.

The organized smaller structures around the coherent vortex are instrumental in scalar mixing and entrainment. The predominant azimuthal alignment of the secondary structures implies that they can induce a local flow with a significant radial velocity. An example of this is seen in Fig. 18, which shows both vorticity magnitude and scalar concentration at the end ($t^*=8$) of simulation $T6$. Two secondary structures with opposite polarization are indicated in Fig. 18(A). We clearly observe how fluid from outside with low scalar concentration is transported radially inwards between two structures, while at the edges of the pair, fluid with high scalar concentration is convected radially outwards. Thus, azimuthally aligned structures contribute to entrainment and scalar mixing. Finally, note that the vortical structures in the surrounding layer are not directly marked by the scalar, but can be only qualitatively inferred from the scalar concentration.

VIII. DISCUSSION AND CONCLUSION

A. A conjecture about local anisotropy

Traditionally, turbulence theory invokes the assumption of local isotropy for scales in the inertial subrange, thus assuming that there is no preferred direction of the vorticity associated with scales which are both much larger than the Komolgorov scale and much smaller than the energy containing integral scale. Consequently in the limit of infinite Reynolds number, anisotropy is only associated with the large scales of the flow. Note that the assumption of local isotropy does not imply that there are no structures in the inertial subrange, nor does it imply anything about the shape of such structures. What it does imply, however, is that the orientation of small-scale structures is statistically random. Local isotropy is indeed a strong assumption, which, however, is very convenient for calculating the transfer of energy between different scales. In essence local isotropy implies a decoupling of large and fine scales. As mentioned by Hussain [1], the evolutions of large and fine scales might be intimately coupled, thus suggesting that local isotropy is suspect in turbulent shear flows. With basis in the results obtained here we pursue this idea further by formulating the conjecture that a coherent structure will induce local anisotropy at all scales in its vicinity. We also present a physical space picture of how the cascade of energy from larger to smaller scales might take place.

The presence of the coherent vortex clearly makes the large scales anisotropic. We will now examine how the anisotropy of the largest scales cascades down to the smallest scales. The first step in this cascade is discussed above, namely, that the coherent vortex gives rise to the formation of secondary vortical structures (threads) in the surrounding layer (e.g., Fig. 4) through alignment and subsequent amalgamation of small-scale structures. These secondary structures may then, provided that they are sufficiently strong, dominate the strain rates in their immediate vicinity. If the Reynolds number is sufficiently

large, so as to allow the existence of even smaller scales, we can then imagine that these smaller scales align and organize azimuthally around the threads, as shown in Fig. 19(A). In the limit of infinite Reynolds number, this line of reasoning leads to a hierarchy of increasingly smaller scale structures which are organized as schematically suggested in Figs. 19(A)–19(C). By construction this figure represents a fractal vortical structure. The notion of fractals in turbulence is not new; it can in fact be traced back to Richardson [18] and has been promoted extensively by Mandelbrot [19,20]. The present scenario merely adds a concrete physical space picture. An interesting aspect of the fractal vortex shown in Fig. 19 is

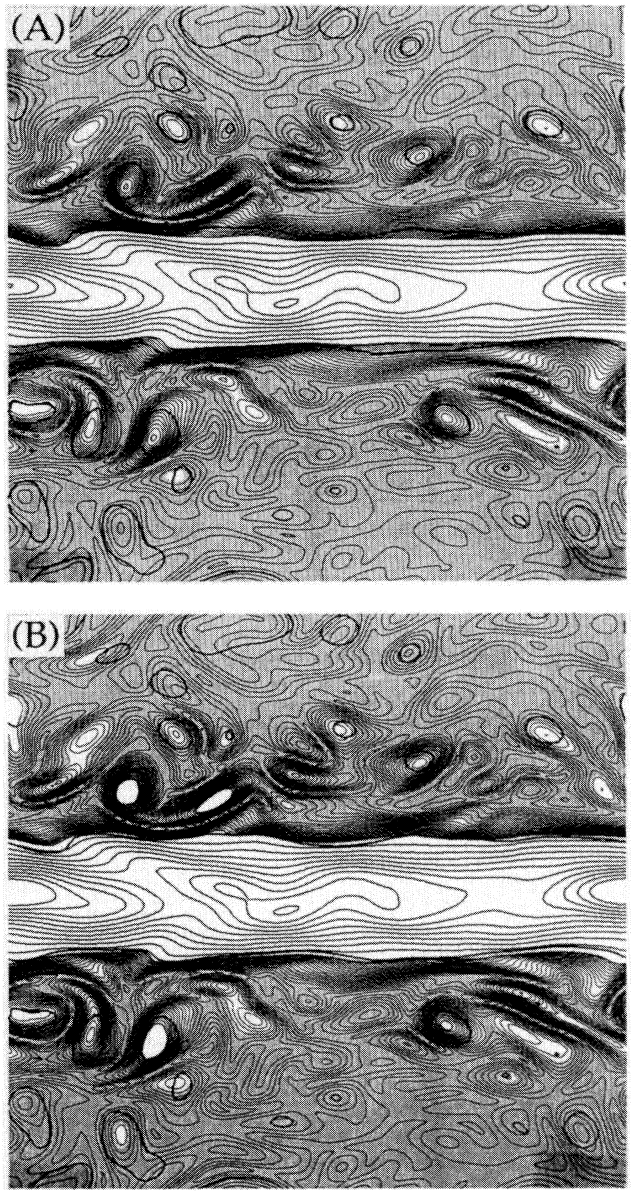

FIG. 16. Contours of the vorticity norm in $\pi_{\|}$ at the end of simulations $T9$ (a) and $T10$ (b). The contour levels in the two panels are equal. The lowest contour levels are shaded gray. Moreover, a smaller contour increment has been used for the lower levels (up to 30% of the peak) than for the high levels.

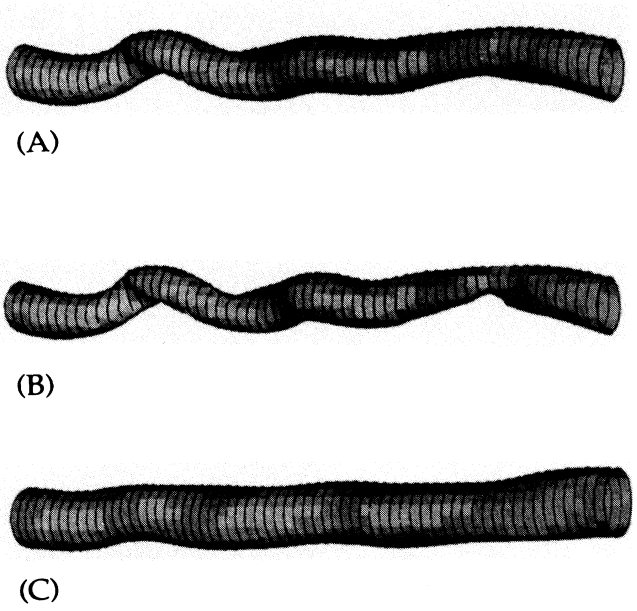

FIG. 17. 65% level isovorticity surfaces at the end of simulations $T9$ (A) and $T10$ (B). Comparison with the end of simulation $T5$ (C), the initial condition of simulations $T9$ and $T10$, shows the excitation of bending waves.

that the spatial support of the dissipation might also be fractal, or multifractal. Note that the present simulations have Reynolds numbers which are too low to reveal more than the secondary structures, and thus the existence of a hierarchy of small-scale structures is purely a speculation. However, if this speculative scenario has merit, then it follows that a coherent structure induces a departure from local isotropy directly at all scales.

A few remarks about such a fractal vortical structure are in order. First, the structure would not be stationary, but constantly changing although it may still be statistically stationary. For example, each time two secondary structures of the same polarization pair, or each time two secondary structures of opposite polarity come in close proximity, a subsequent rearrangement of the accompanying smaller-scale structures would follow, presumably much the same way as the "ribs" rearrange following pairings of "rolls" in a mixing layer. Second, the time scale associated with the smaller vortical structures decreases in proportion to the size of the structures, thereby enabling the smaller-scale structures to adjust rapidly to changes in the larger-scale structures. Third, the inherent local anisotropy would not necessarily make the flow unamenable to modeling, for the role played by the local isotropy assumption would be replaced by a fractal self-similarity in the surrounding layer. Fourth, the fractal vortical structure would give a clear physical space picture of how the energy cascade from large to small scales takes place, for the secondary structures take energy from the coherent vortex, and so on.

B. Comparison with other "spiral-type" intermittency scenarios

The spiral small-scale structures surrounding our coherent structure constitute an alternative type of inter-

nal intermittency. It has some features in common with Lundgren's model [10] as well as with Childress model [11]. However, there are also many differences. Here we compare the different scenarios and also discuss what effect axial straining would have on our structure.

Lundgren [10] conjectures a spiral-type intermittency near a columnar vortex which is subject to axisymmetric axial stretching. A noticeable feature of this model is that it yields a $-\frac{5}{3}$ spectrum. In Lundgren's model, the vorticity is everywhere parallel to the axis of the vortex

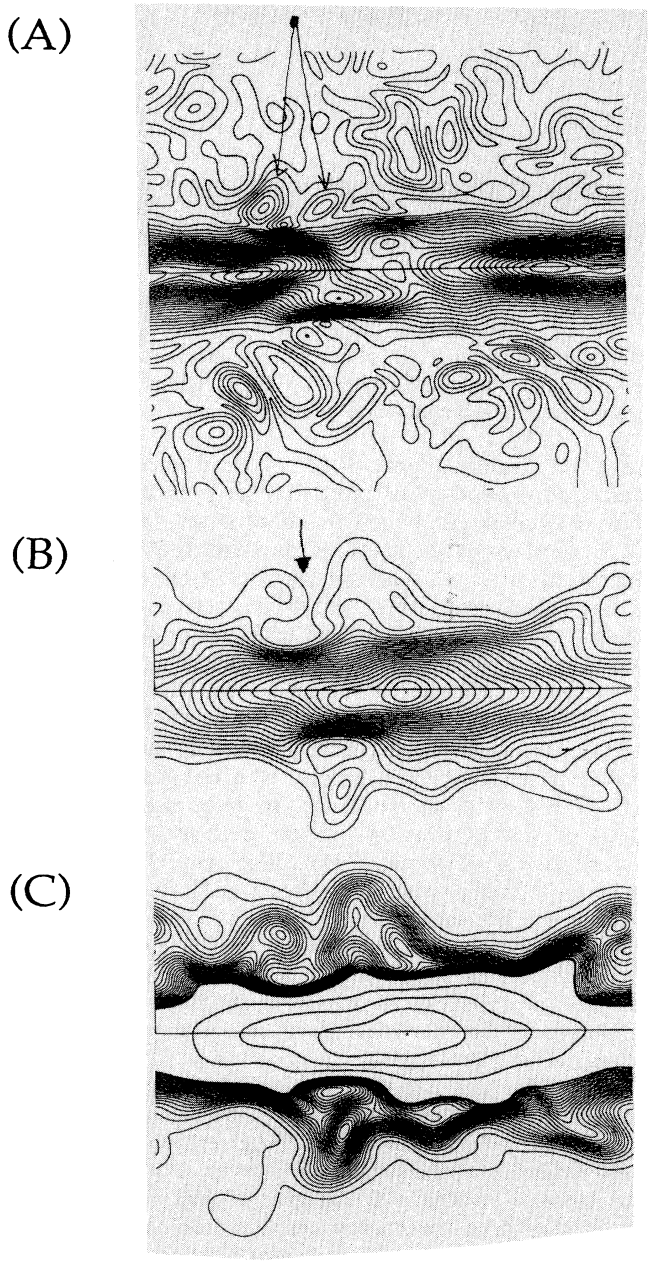

FIG. 18. Scalar entrainment due the small-scale vortical structures in the surrounding layer for the last frame of simulation $T6$. (A) Contours of the vorticity norm in $\pi_{\|}$. (B) Contours of the scalar concentration, which initially matched the distribution of $\xi_{r=\infty}-\xi$ (here $\xi \equiv rv_\theta$) in the axisymmetric coherent vortex. (C) Scalar contours in the lowest 20% level.

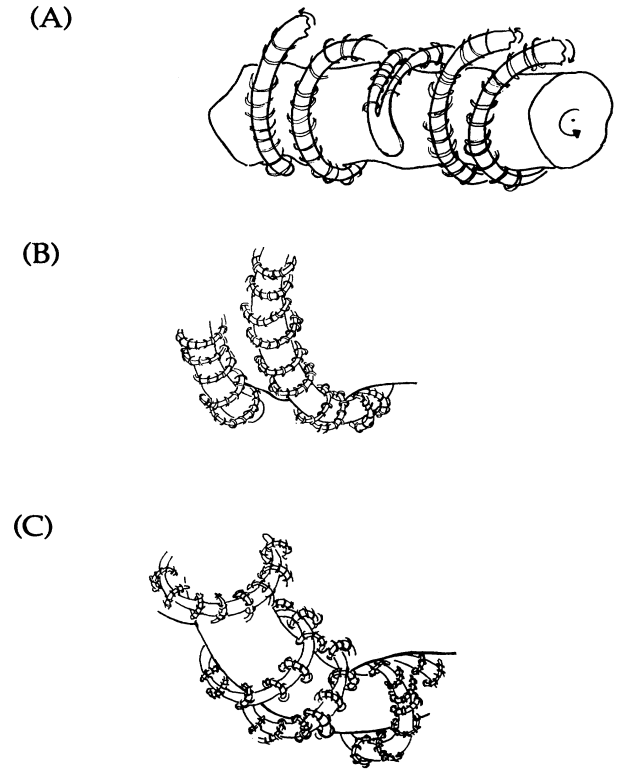

FIG. 19. Schematic illustrating our conjecture of a fractal vortex in the high-Reynolds-number limit. Frames (A)–(C) show successive magnifications.

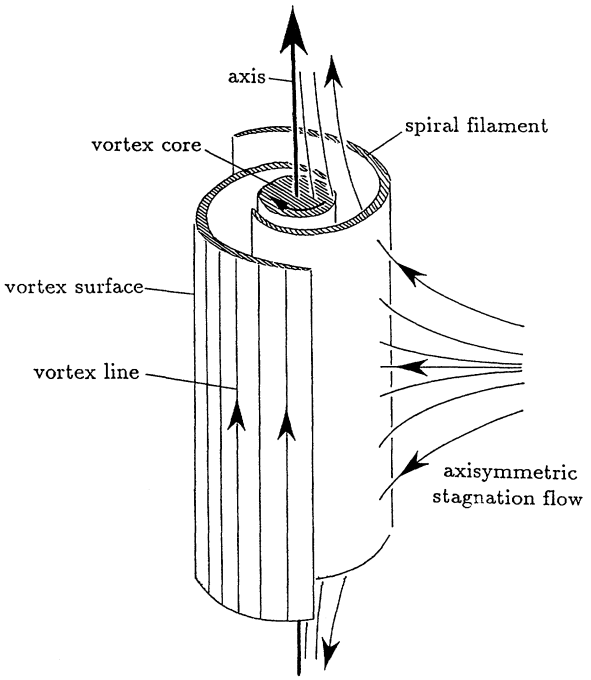

FIG. 20. Schematic of a Lundgren vortex [10].

(i.e., the z axis)—even in the spiral structure; see Fig. 20. Lundgren shows that the dynamics of the vortex can be transformed to that of a two-dimensional vortex [Eqs. (11) and (12) in Ref. [10]]. Thus, spiral structures typically result from the two-dimensional mechanism known as axisymmetrization [3], where a noncircular vortex spins off filaments, in the form of spiral arms, so as to make the core region circular. The Lundgren vortices differ from regular two-dimensional vortices through the axial stretching, which makes the filaments much thinner than in two-dimensional vortex dynamics. These thin filaments are the source of the $-\frac{5}{3}$ spectrum.

Our intermittent structure differs from Lundgrens in four ways. First, our coherent structure is not subject to external axial stretching, but only to local internal axial stretching resulting from the core dynamics. Second, our small scales are primarily recruited from the turbulent environment of the coherent vortex, whereas Lundgrens spirals are expelled from an initially noncircular vortex core. Third, the vorticity in our small-scale structures is essentially perpendicular to the axis of the coherent vortex—in Lundgren's spirals the vorticity is parallel to the axis of the vortex. Finally, our small scales are polarized and have high helicity, while Lundgren's are unpolarized and have no helicity.

In the presence of axisymmetric axial stretching our intermittent structure may or may not develop—the deciding factor is the ratio between the initial mean vorticity in the vortex $\bar{\omega}(0)$ and the axial strain rate S. In the Appendix we consider the passive advection of a material curve in the flow of an axial stretched potential vortex. We find that the curve will ultimately align with the axis of the vortex when $S>0$. However, if $\bar{\omega}(0)/S \gg 1$ many vortex turnover times elapse before the ultimate axial alignment sets in, and meanwhile the material curve aligns azimuthally. Based on these considerations, we conclude that our intermittent structure will also form in the presence of weak axial stretching.

The vortex tube cascade model of Childress [11] results in a fully three-dimensional fractal vortex structure, which resembles our Fig. 19. As in our case the small scales have helicity. However, the intermittent structure is generated by a different mechanism, namely, through instability of the vortex core, and not as in our case through the recruitment of fine scales from a turbulent environment. In this respect the Childress model, like Lundgren's, provides a physical space description of how a cascade can build up. Our scenario does not describe the build up of a cascade, but elucidates the coexistence of a coherent structure and surrounding turbulence. That is, we describe how the turbulent environment is affected and organized by the presence of a large-scale tubular vortex.

C. Summary of results and future directions

When the laminar vortex is superimposed on fine-scale turbulence we have a prototype of a segment of a coherent structure in a turbulent flow as well as of internal intermittency near a strong vortical structure. The coherent vortex induces a very special type of intermittency in the surrounding layer. The vorticity in this layer is organized in spiral patterns and is almost parallel or antiparallel to the swirl of the coherent vortex. This way the vorticity dynamics in the surrounding layer is subjected to some of the same constraints as 2D turbulence. In particular, we have identified pairings between structures with vorticity oriented in the same direction as a frequent event, which in fact organizes small vortical structures in the surrounding layer into larger ones. An important feature of the small-scale structures is that they tend to be highly polarized, i.e., left or right handed. Such polarization partially suppresses energy cascades to larger wave numbers.

In spite of the observed pairings, we have not found an inverse energy cascade. On the contrary, the energy transfer is always from larger to smaller scales. This is because the small scales are energized at the expense of the coherent vortex. Even when the small-scale vortical structures in the surrounding layer are very weak compared to the coherent vortex, they have the potential for making the vortex fully turbulent provided that the Reynolds number is sufficiently high. Thereby, the small scales can have a profound impact on the coherent vortex itself, an effect which cannot be modeled by any type of eddy viscosity. This feedback consists of the excitation of bending waves on the coherent vortex. Another effect of the small scales on the coherent vortex is a quicker expansion of the vortex core and the associated reduction of the vorticity magnitude; the latter has the consequence that the core dynamics is slower than in the laminar case. This effect can conceivably be modeled by an enhanced diffusion.

This paper opens up several new directions for future research into coherent structure dynamics and turbulence. To a large extent, these center around the helical-wave decomposition, the dynamics of the polarized vorticity components in turbulent flows, and the evolution and interaction of isolated vortices of high polarization. The reasons why these issues demand further consideration are that the polarized vorticity components give detailed insight into vortex dynamics, and the observation that 3D vortical structures in general are polarized. Some flows such as the circular jet are not initially truly 3D but axisymmetric. However, after a circular jet has undergone rollup and successive pairings, and the ring structures develop azimuthal instabilities, then the polarized vorticity components start to separate spatially. It is here important to realize that the ring instabilities consist entirely of core dynamics. When the ring structures break down completely, and the jet becomes fully turbulent, then the flow field consists of mainly streamwise vortical structures, which have the form of lobes or asymmetric hairpins. These structures are each partially polarized, i.e., one leg in a hairpin is predominantly right handed while the other is predominantly left handed [21]. It remains to be seen if the transition to turbulence in general is coupled to the spatial separation of the polarized vorticity components. The separation also occurs during asymmetric collision of vortex rings and in a viscous flow is a principal mechanism for generation of total helicity H and making the flow approach a Beltrami

state [22]. A natural continuation of the present paper is therefore to analyze the structure of the internal intermittency near a fully or partially polarized vortical structure. Presumably, the small-scale structures surrounding the vortex will have a corkscrew structure, be wrapped around the vortex, and have the same polarization as the coherent vortex.

ACKNOWLEDGMENTS

This research has been supported by the Office of Naval Research under Grant No. N00014-89-J-1361 and the Air Force Office of Scientific Research under Grant No. F49620-92-J-0200.

APPENDIX: ALIGNMENT OF A PASSIVE MATERIAL CURVE

Consider an inviscid column vortex subject to axial stretching;

$$v_r=-\frac{S}{2}r,\quad v_\theta=\frac{\Gamma}{2\pi r},\quad v_z=Sz\ , \tag{A1}$$

here Γ is the circulation and S is the constant strain rate. The trajectory of a particle α is given by

$$\begin{aligned} r_\alpha(t)&=r_\alpha(0)\exp\left[-\frac{St}{2}\right]\ ,\\ \theta_\alpha(t)&=\frac{\Gamma}{2\pi S r_\alpha^2(0)}(e^{St}-1)+\theta_\alpha(0)\ ,\\ z_\alpha(t)&=z_\alpha(0)e^{St}\ . \end{aligned} \tag{A2}$$

Now consider two particles, α and α', which are very close together at $t=0$. The separation between these particles is

$$\begin{aligned} \delta r(t)&=r_{\alpha'}(t)-r_\alpha(t)\ ,\\ \delta\theta(t)&=\theta_{\alpha'}(t)-\theta_\alpha(t)\ ,\\ \delta z(t)&=z_{\alpha'}(t)-z_\alpha(t)\ . \end{aligned} \tag{A3}$$

Using (A2) we find

$$\begin{aligned} \delta r(t)&=\delta r(0)e^{-St/2}\ ,\\ \delta\theta(t)&=\delta\theta(0)+\frac{\Gamma}{\pi S r_\alpha^3(0)}\delta r(0)(1-e^{St})\ ,\\ \delta z(t)&=\delta z(0)e^{St}\ . \end{aligned} \tag{A4}$$

Now let α and α' be particles on a material line which is advected by the flow (A1). The tangent direction $\mathbf{s}$ of the line at the material particle α changes with time in a manner, which we can easily calculate from (A4). The tangent direction can be described in terms of three angles: ϕ_{rz}, $\phi_{\theta z}$, and $\phi_{r\theta}$. These angles are defined such that

$$\begin{aligned} \tan\phi_{rz}&=\frac{\mathbf{e}_z\cdot\mathbf{s}}{\mathbf{e}_r\cdot\mathbf{s}}\ ,\\ \tan\phi_{\theta z}&=\frac{\mathbf{e}_z\cdot\mathbf{s}}{\mathbf{e}_\theta\cdot\mathbf{s}}\ ,\\ \tan\phi_{r\theta}&=\frac{\mathbf{e}_\theta\cdot\mathbf{s}}{\mathbf{e}_r\cdot\mathbf{s}}\ . \end{aligned} \tag{A5}$$

Using (A4) and taking the limit $\alpha'\to\alpha$ we find

$$\tan\phi_{rz}(t)=\lim_{\alpha'\to\alpha}\frac{\delta z(t)}{\delta r(t)}=\lim_{\alpha'\to\alpha}\frac{\delta z(0)}{\delta r(0)}e^{St/2}=e^{St/2}\tan\phi_{rz}(0)\ , \tag{A6}$$

$$\begin{aligned} \cot\phi_{\theta z}(t)&=\lim_{\alpha'\to\alpha}\frac{r_\alpha(t)\delta\theta(t)}{\delta z(t)}\\ &=\lim_{\alpha'\to\alpha}\left[e^{-3St/2}\frac{r_\alpha(0)\delta\theta(0)}{\delta z(0)}-\frac{\Gamma}{\pi S r_\alpha^2(0)}e^{-St/2}(1-e^{-St})\frac{\delta r(0)}{\delta z(0)}\right]\\ &=e^{-3St/2}\cot\phi_{\theta z}(0)-\frac{\Gamma}{\pi S r_\alpha^2(0)}e^{-St/2}(1-e^{-St})\cot\phi_{rz}(0)\ , \end{aligned} \tag{A7}$$

$$\begin{aligned} \tan\phi_{r\theta}(t)&=\lim_{\alpha'\to\alpha}\frac{r_\alpha(t)\delta\theta(t)}{\delta r(t)}=\lim_{\alpha'\to\alpha}\left[\frac{r_\alpha(0)\delta\theta(0)}{\delta r(0)}-\frac{\Gamma}{\pi S r_\alpha^2(0)}(e^{St}-1)\right]\\ &=\tan\phi_{r\theta}(0)-\frac{\Gamma}{\pi S r_\alpha^2(0)}(e^{St}-1)\ . \end{aligned} \tag{A8}$$

Note the two obvious cases: (1) if $\mathbf{s}$ is initially normal to the radial direction then $\mathbf{s}$ remains so; (2) if $\mathbf{s}$ is initially normal to the axial direction then $\mathbf{s}$ stays that way. Excluding these two cases, all the trigonometric functions in (A6)–(A8) are nonsingular. We notice immediately that in the limit of large St, the tangent will align with the z axis. However, formula (A7) shows that substantial azimuthal alignment ($\phi_{\theta z}\approx 0$) can occur first. This is because of the second term in the final expression (A7). This term involves the factor $\exp(-St/2)[1-\exp(-St)]$ which is initially zero, but then increases to a maximum of $2/27^{0.5}\approx 0.38$ at $St=\ln 3\approx 1.1$ before its final montonic decay. Moreover, this term includes the factor $\Gamma/\pi S r_\alpha^2(0)$ which is of order $\bar{\omega}/S$ ($\bar{\omega}$ is the mean initial vorticity of the vortex core) when $r_\alpha(0)$ is comparable to the initial core size. Thus, for $S/\bar{\omega}\ll 1$ many turnover times will elapse before t reaches the value $(\ln 3)/S$, and hence before the axial alignment sets in. Prior to $t=(\ln 3)/S$ (A7) shows azimuthal alignment, which is substantial for $S/\bar{\omega}\ll 1$. When $St\ll 1$, the asymptotic form of (A7) is

$$\cot\phi_{\theta z}(t)=\cot\phi_{\theta z}(0)-\frac{\Gamma t}{\pi r_\alpha^2(0)}\cot\phi_{rz}(0)$$

$$=\cot\phi_{\theta z}(0)-t\bar{\omega}\frac{\sigma^2}{r_\alpha^2(0)}\cot\phi_{rz}(0)\ , \qquad \text{(A9)}$$

where σ is the initial vortex core size.

The above analysis shows that the alignment of a passive material curve involves two distinct phases when the axial straining is weak: first, an intermediate azimuthal alignment phase ($St<1$), then the terminal axial alignment ($St>1$).

[1] F. Hussain, in *Turbulence and Chaotic Phenomena in Fluids,* edited by T. Tatsumi (North-Holland, Amsterdam, 1984), p. 245.

[2] F. Hussain, J. Fluid Mech. **173**, 303 (1986).

[3] M. V. Melander, J. C. McWilliams, and N. J. Zabusky, J. Fluid Mech. **178**, 137 (1987).

[4] J. C. McWilliams, J. Fluid Mech. **146**, 21 (1984).

[5] A. Babiano, C. Basdevant, B. Legras, and R. Sadourny, J. Fluid Mech. **183**, 379 (1987).

[6] F. K. Browand and P. D. Weidman, J. Fluid Mech. **76**, 127 (1976).

[7] K. B. M. Q. Zaman and A. K. M. F. Hussain, J. Fluid Mech. **101**, 449 (1980).

[8] G. L. Brown and A. Roshko, J. Fluid Mech. **64**, 775 (1974).

[9] S. C. Crow and F. H. Champagne, J. Fluid Mech. **48**, 549 (1971).

[10] T. S. Lundgren, Phys. Fluids **25**, 2193 (1982).

[11] S. Childress, Geophys. Astrophys. Fluid Dyn. **29**, 29 (1984).

[12] M. V. Melander and F. Hussain, Fluid Dyn. Res. (to be published).

[13] M. V. Melander and F. Hussain, Phys. Fluids A **5**, 1992 (1993).

[14] M. van Dyke, *An Album of Fluid Motion* (Parabolic, Stanford, 1988).

[15] S. Taneda, Prog. Aero. Sci. **17**, 287 (1977).

[16] M. Lesieur, *Turbulence in Fluids,* 2nd ed. (Kluwer Academic, Dordrecht, 1990).

[17] M. V. Melander, N. J. Zabusky, and J. C. McWilliams, J. Fluid Mech. **195**, 303 (1988).

[18] L. F. Richardson, Proc. R. Soc. London, Ser. A **110**, 709 (1926).

[19] B. Mandelbrot, J. Fluid Mech. **62**, 331 (1974).

[20] B. Mandelbrot, *The Fractal Geometry of Nature* (Freeman, San Francisco, 1982).

[21] M. V. Melander, F. Hussain and A. Basu, in *Proceedings of the 8th Symposium on Turb Shear Flows,* Munich, 1991, edited by F. Durst *et al.* (University of Munich, Munich, 1991), p. 15-5.

[22] F. Hussain and M. V. Melander, in *Topological Aspects of the Dynamics of Fluids and Plasma,* edited by H. K. Moffatt *et al.* (Kluwer, Dordrecht, 1992), p. 377.

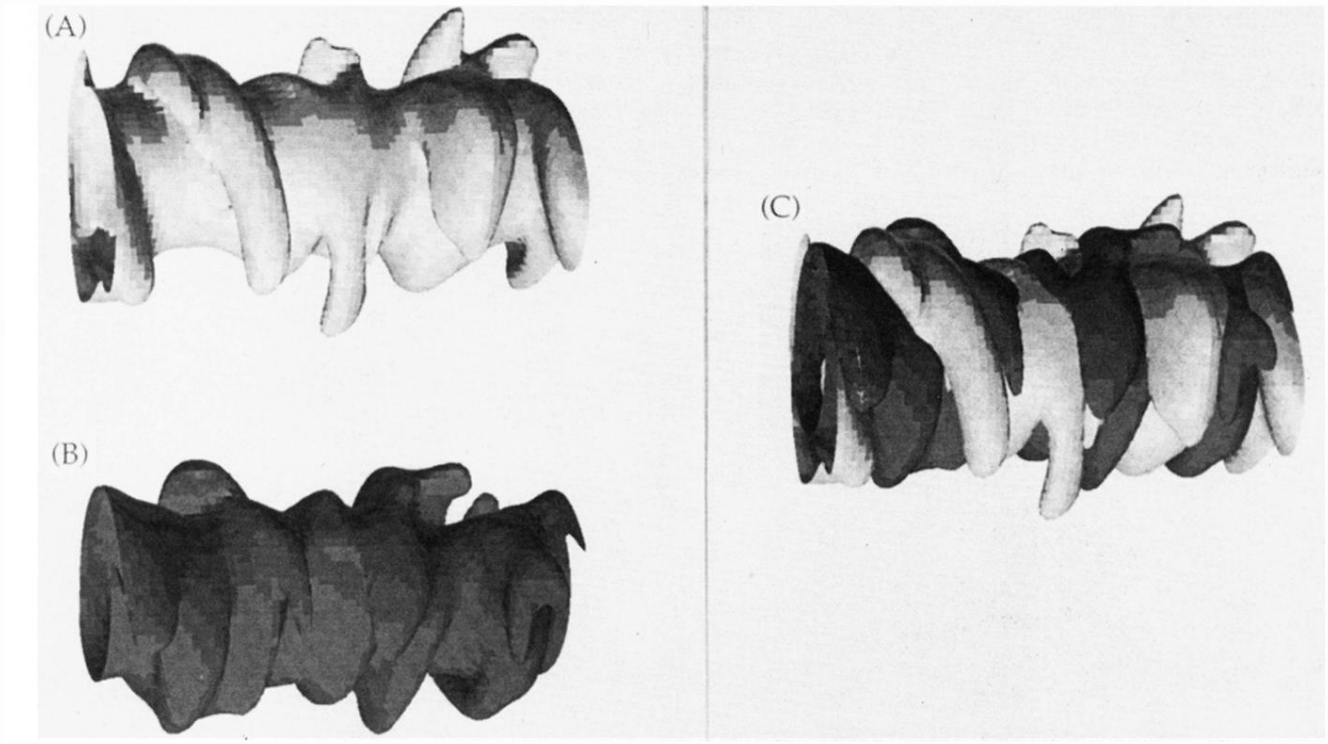

FIG. 10. Isovorticity surfaces of the polarized vorticity components corresponding to frame (q) of Fig. 3. The light-shaded surface is the right-handed contribution (A), the dark-shaded surface is the left-handed one (B). The overlay of the two is shown in (C).

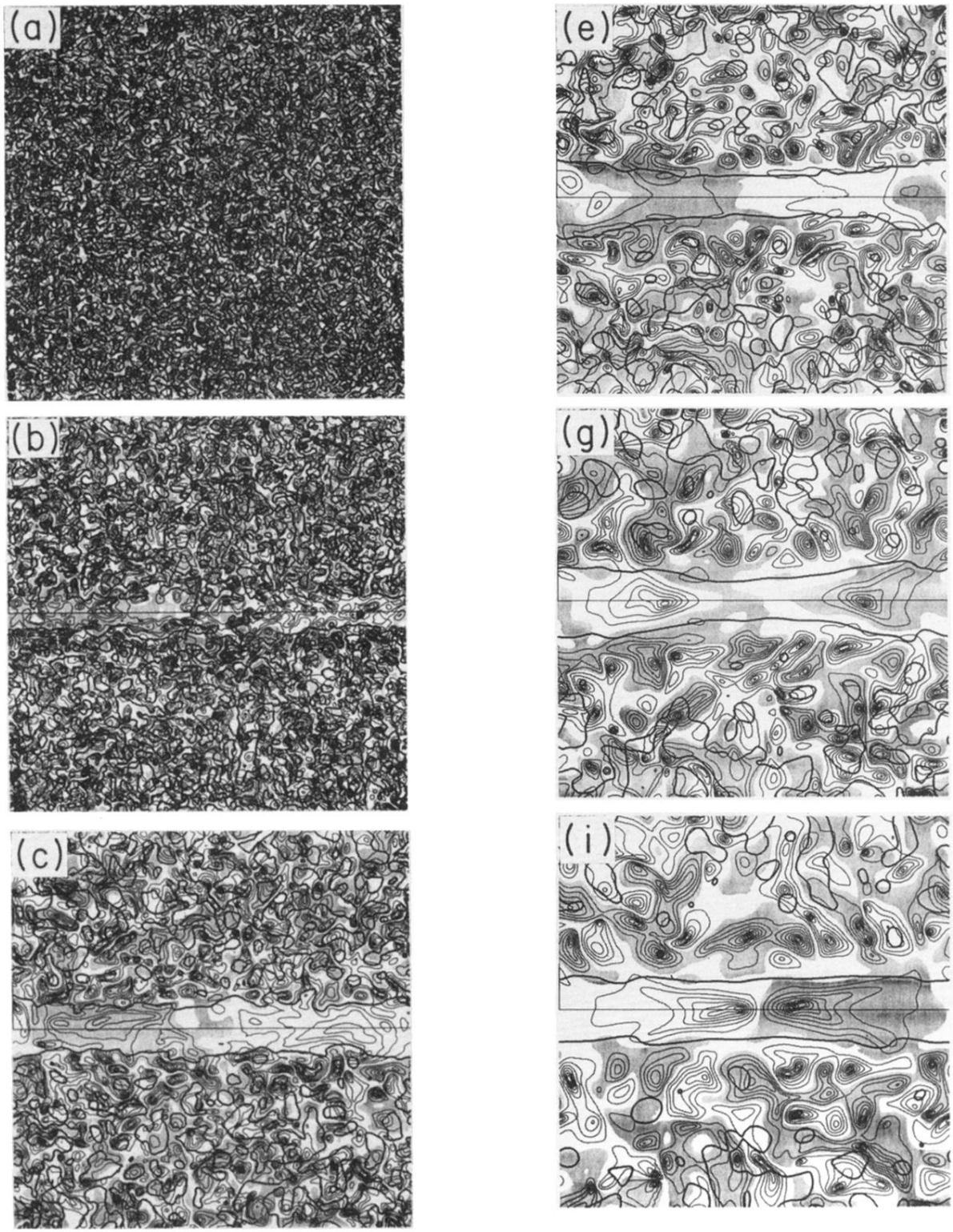

FIG. 11. Pointwise polarization ratio $\mathcal{R}$ [defined in Eq. (2)] for case $T5$ is shown in plane $\pi_{\|}$ at times given in Table III. Contour levels are in increments of 0.5 and the negative values are marked by gray shading. For reference the $\mathfrak{W}_k = 1$ contour is overlaid with a heavy line in each frame.

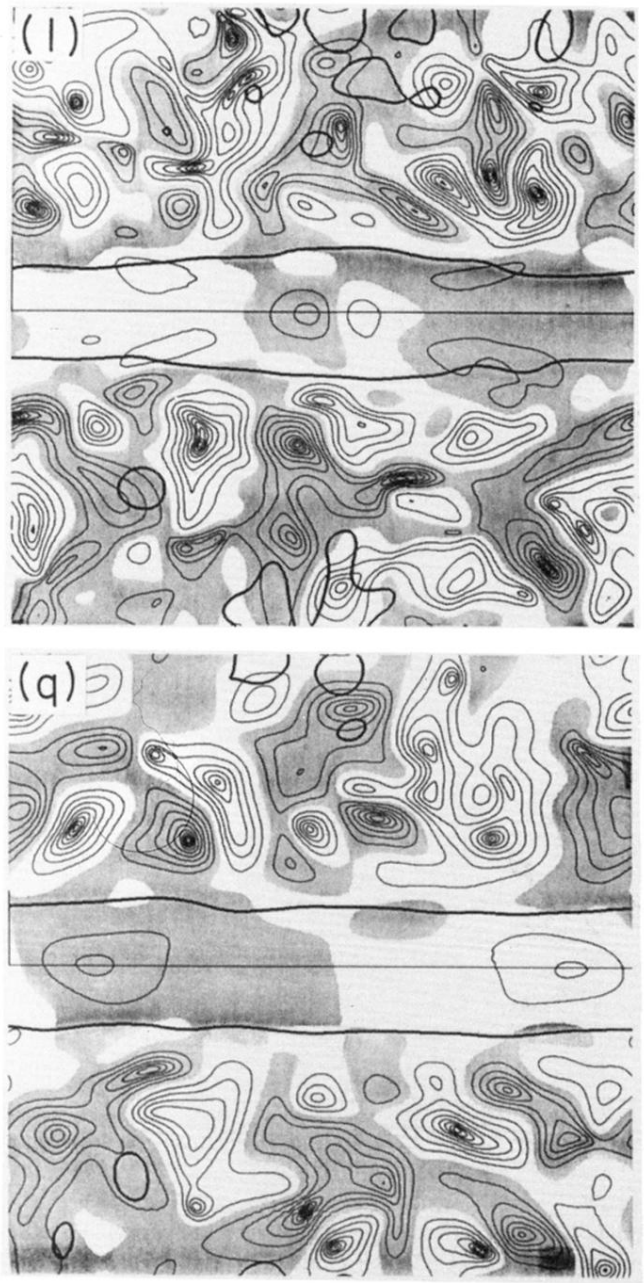

FIG. 11. (*Continued*).

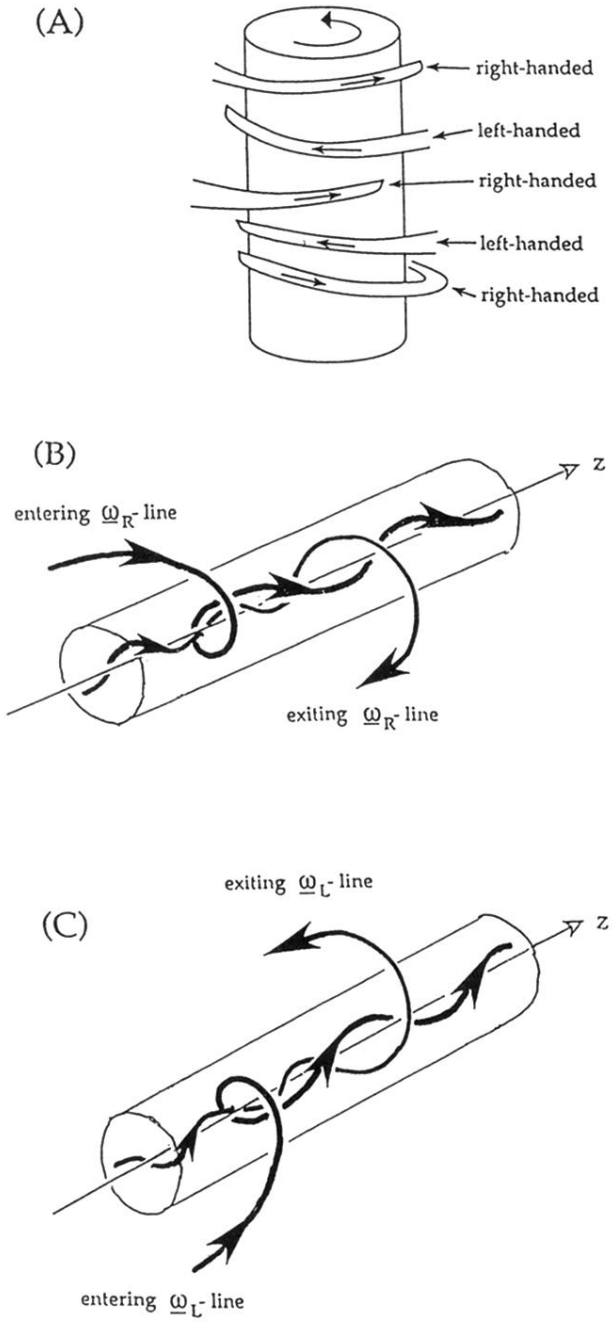

FIG. 12. (A) Sketch of the general orientation of the left- and right-handed small-scale vortical structures surrounding the coherent vortex. (B) Sketch of the right-handed vorticity components vector lines. (C) Sketch of the left-handed vorticity components vector lines. (D) Contours of normal component of $\boldsymbol{\omega}_R$ in $\pi_{\|}$. (E) Contours of normal component of $\boldsymbol{\omega}_L$ in $\pi_{\|}$. (F) Highly localized coiling of vector lines. (G) Contours of the helicity density $h = \mathbf{u}\cdot\boldsymbol{\omega}$ in $\pi_{\|}$.

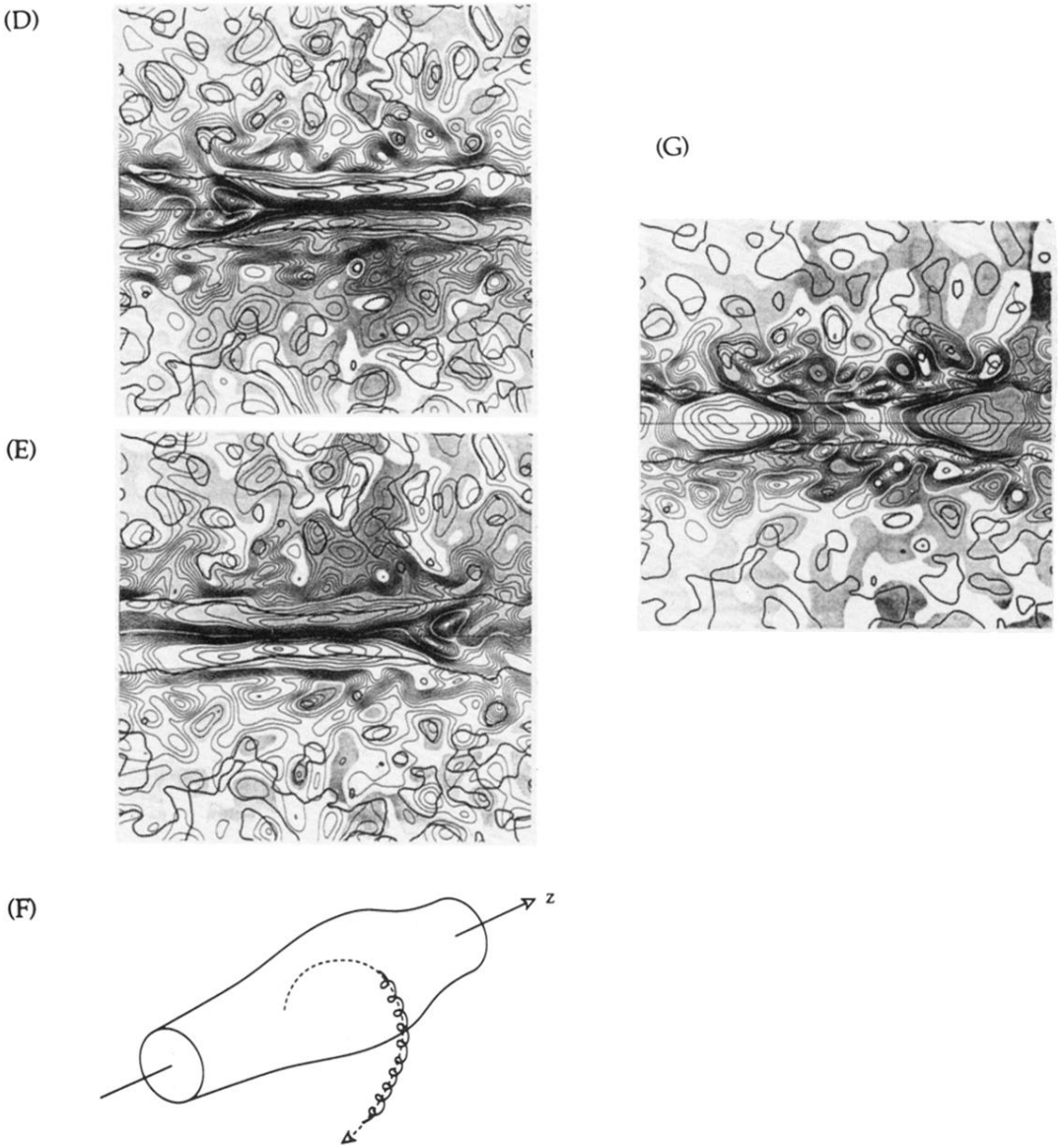

FIG. 12. (*Continued*).

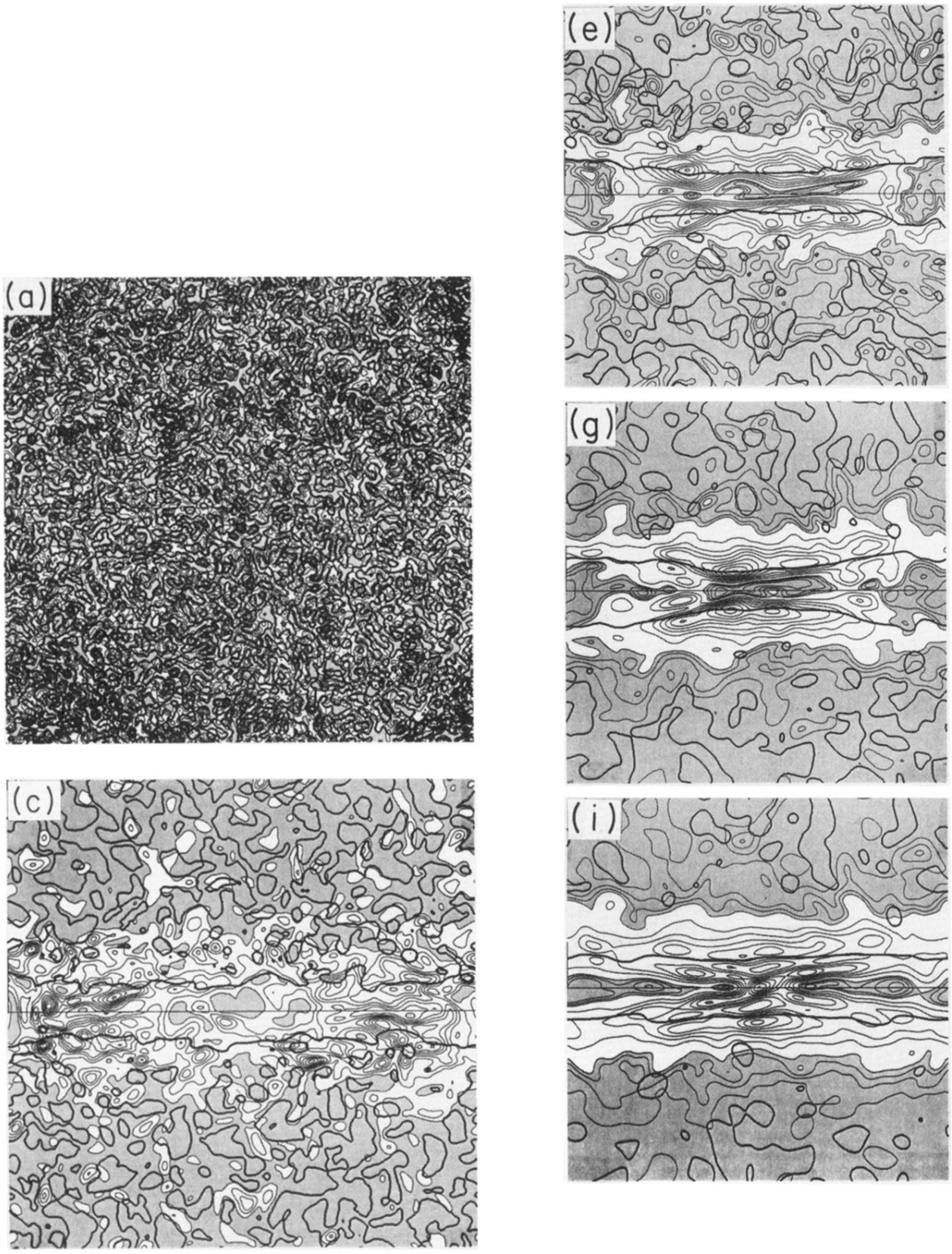

FIG. 13. Contours of dissipation in the plane $\pi_{\|}$ for case $T5$ at times given in Table III. The contour levels are in dimensional units: (a) $\epsilon_h = 3000$, $\delta\epsilon = 300$, gray shading for $\epsilon < 600$; (c) $\epsilon_h = 3.6$, $\delta\epsilon = 0.4$, gray shading for $\epsilon < 0.4$; (e) $\epsilon_h = 2.0$, $\delta\epsilon = 0.2$, gray shading for $\epsilon < 0.4$, thin contours are $\epsilon = 0.05,\ 0.1, \ldots, 0.35$; (g) $\epsilon_h = 1.6$, $\delta\epsilon = 0.16$, gray shading for $e < 0.32$, thin contours are $\epsilon = 0.04, 0.08, 0.28$; (i) $\epsilon_h = 0.81$, $\delta\epsilon = 0.09$, gray shading for $\epsilon < 0.18$; (l) $\epsilon_h = 0.4$, $\delta\epsilon = 0.04$, gray shading for $\epsilon < 0.04$, thin contours are $\epsilon = 0.01, 0.02, \ldots, 0.08$; (q) $\epsilon_h = 0.16$, $\delta\epsilon = 0.016$, gray shading for $\epsilon < 0.032$, thin contours are $\epsilon = 0.004, 0.008, 0.012$. For reference the $\mathfrak{W}_k = 1$ contour is overlaid with a heavy line in each frame.

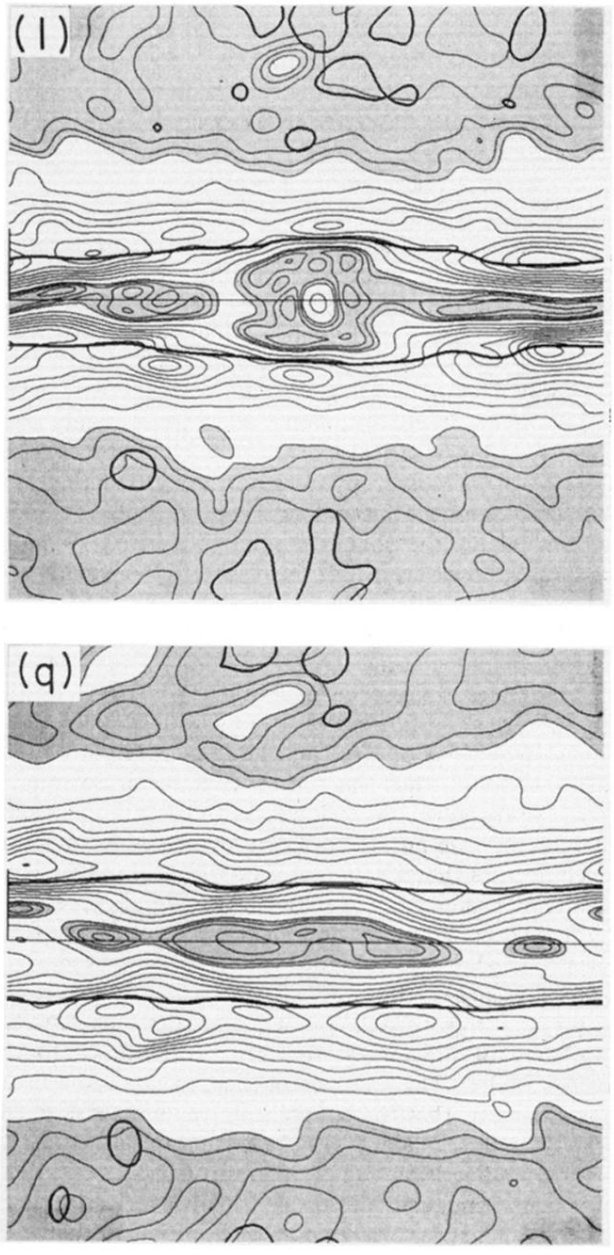

FIG. 13. (*Continued*).

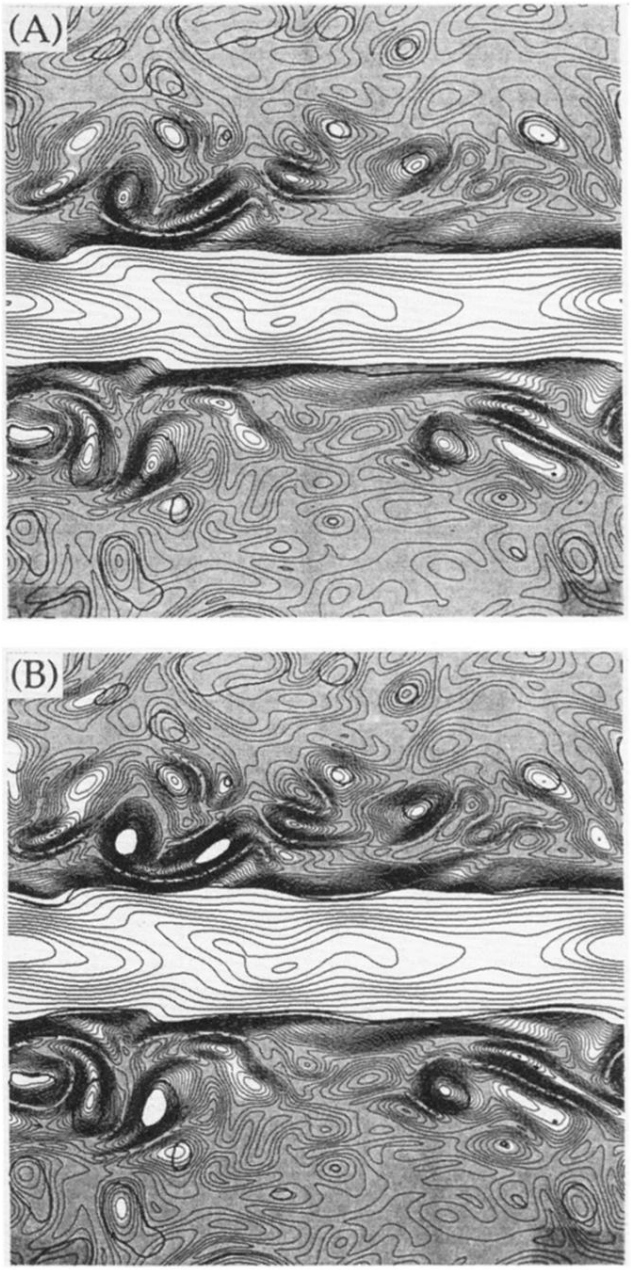

FIG. 16. Contours of the vorticity norm in $\pi_{\|}$ at the end of simulations $T9$ (a) and $T10$ (b). The contour levels in the two panels are equal. The lowest contour levels are shaded gray. Moreover, a smaller contour increment has been used for the lower levels (up to 30% of the peak) than for the high levels.

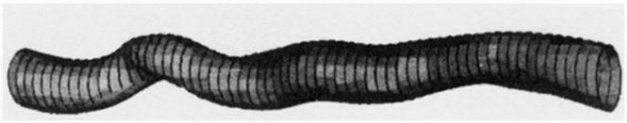

(A)

(B)

(C)

FIG. 17. 65% level isovorticity surfaces at the end of simulations $T9$ (A) and $T10$ (B). Comparison with the end of simulation $T5$ (C), the initial condition of simulations $T9$ and $T10$, shows the excitation of bending waves.

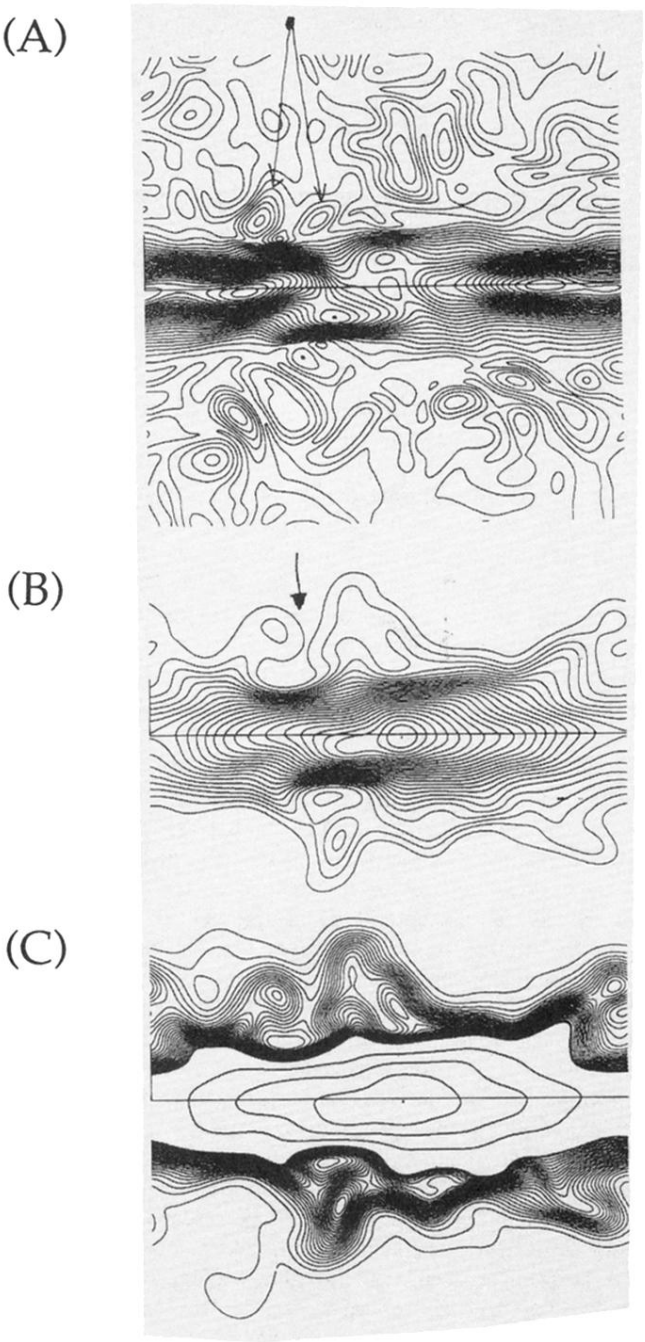

FIG. 18. Scalar entrainment due the small-scale vortical structures in the surrounding layer for the last frame of simulation $T6$. (A) Contours of the vorticity norm in $\pi_{\|}$. (B) Contours of the scalar concentration, which initially matched the distribution of $\xi_{r=\infty}-\xi$ (here $\xi \equiv rv_\theta$) in the axisymmetric coherent vortex. (C) Scalar contours in the lowest 20% level.

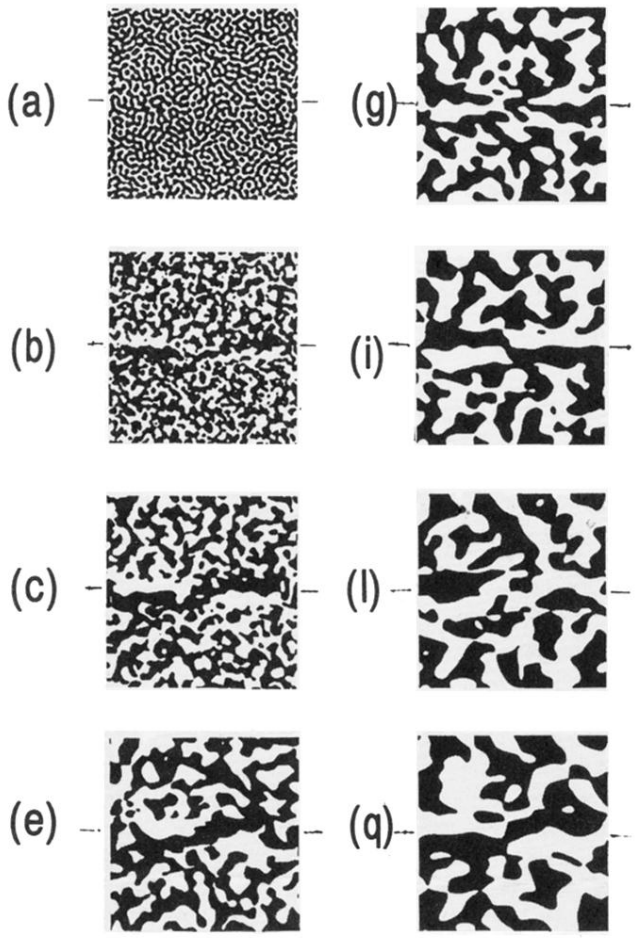

FIG. 2. Positive and negative regions of ω_n in $\pi_\parallel$ for case $T5$ (see Tables I and II). The frame labeling (a), . . . , (q) refers to the times given in Table III; the same labeling is used for same time identification in figures throughout the paper. The horizontal axis of the initially axisymmetric coherent vortex is marked on the side of each frame.

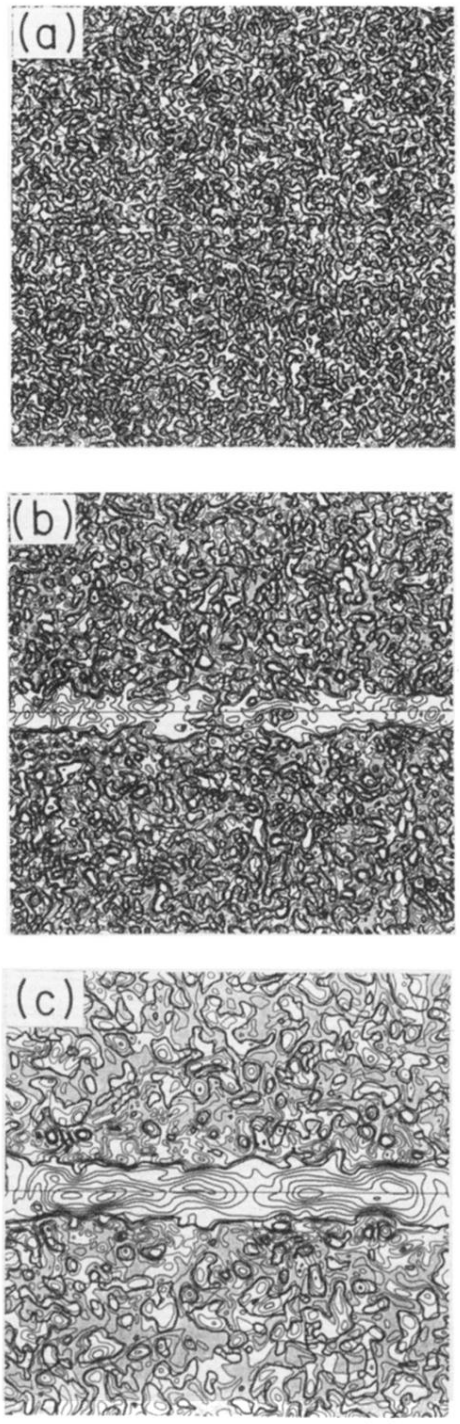

FIG. 3. The vorticity norm in $\pi_{\|}$ for case $T5$ at different times; see Table III. The intersection point of arrows in (g) and (i) indicates the location analyzed later. The contour levels in dimensional units are (a) $\omega_h=70$, $\delta\omega=10$, gray shading for $\omega<10$; (b) $\omega_h=8$, $\delta\omega=1$, gray shading for $\omega<1$, thin contours are for $\omega=0.4,0.8,1.2,1.6$; (c) $\omega_h=4.5$, $\delta\omega=0.5$, gray shading for $\omega<0.4$, thin contours are for $\omega=0.2,0.4,0.8$; (e)–(i) $\omega_h=4.0$, $\delta\omega=0.5$, gray shading for $\omega<0.2$, thin contours are for $\omega=0.05, 0.1, \ldots, 0.45$; (l) $\omega_h=2$, $\delta\omega=0.25$, gray shading for $\omega<0.1$, thin contours are for $\omega=0.02,0.04, \ldots, 0.2$; (q) $\omega_h=1.25$, $\delta\omega=0.25$, gray shading for $\omega<0.1$, thin contours are for $\omega=0.02,0.04, \ldots, 0.2$. For reference the $\mathfrak{W}_k=1$ ($\mathfrak{W}_k\equiv[\omega^2/(2S_{ij}S_{ij})]^{1/2}$ is the kinematic vorticity number) contour is overlaid with a heavy line in each frame.

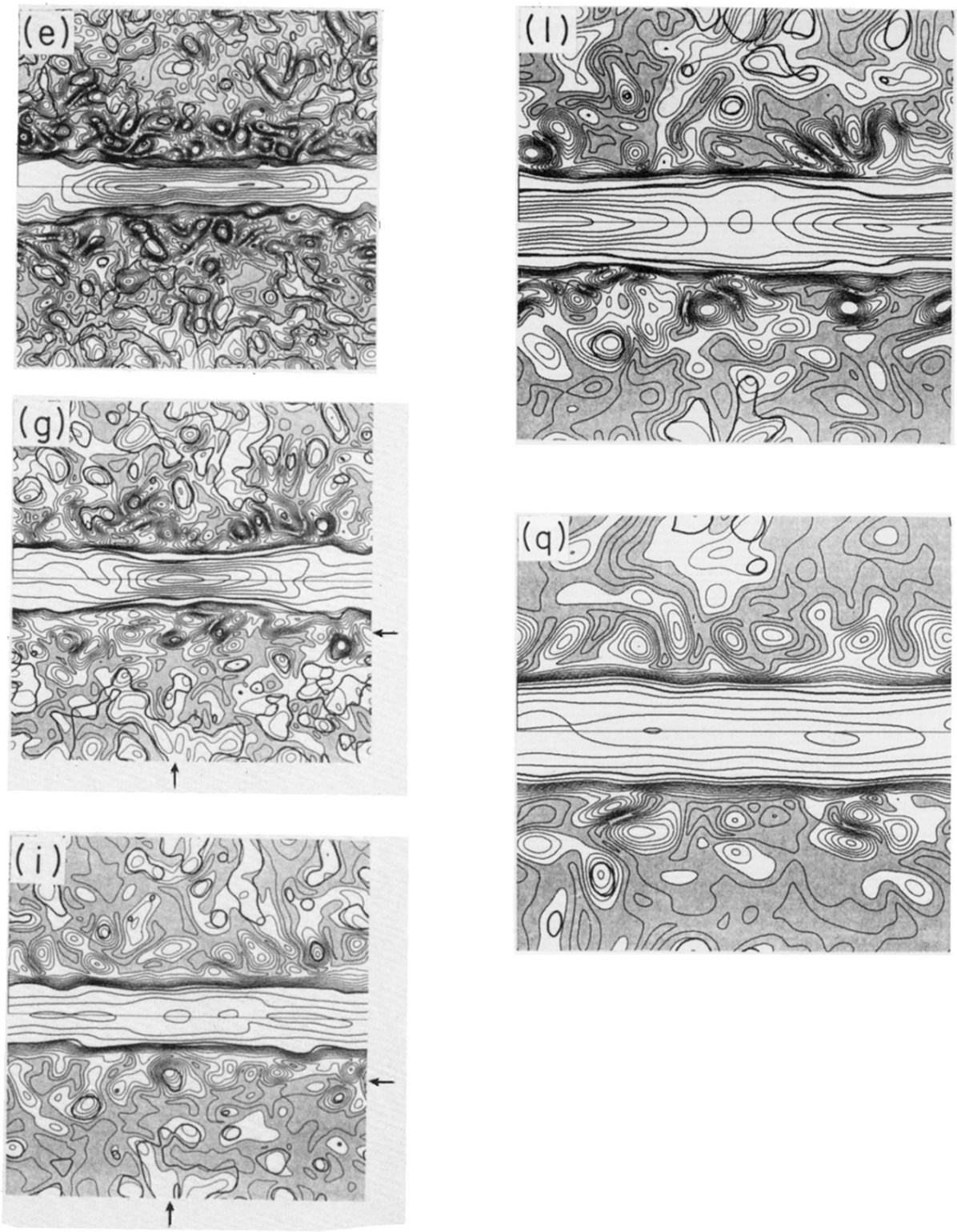

FIG. 3. (*Continued*).

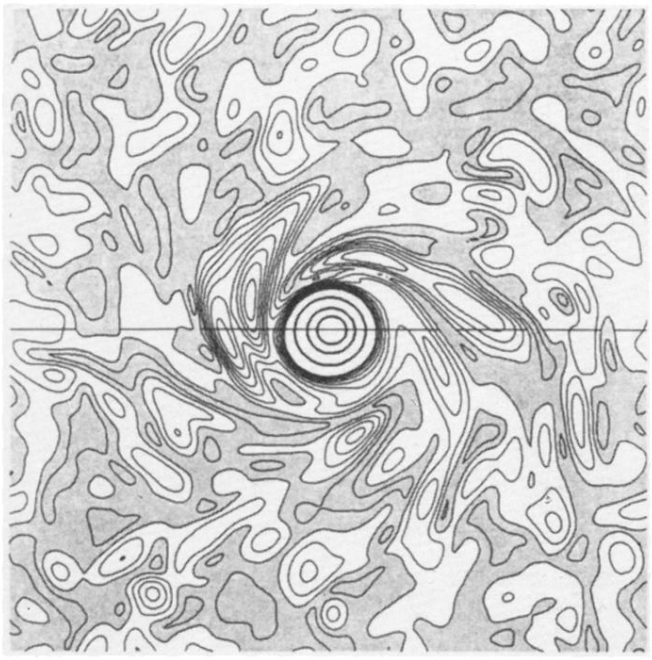

FIG. 4. Cross section of the vortex corresponding to frame (g) of Fig. 3 is shown by the vorticity norm. The lowest contour levels are shaded gray. A smaller contour increment has been used for the low levels than for the high levels.

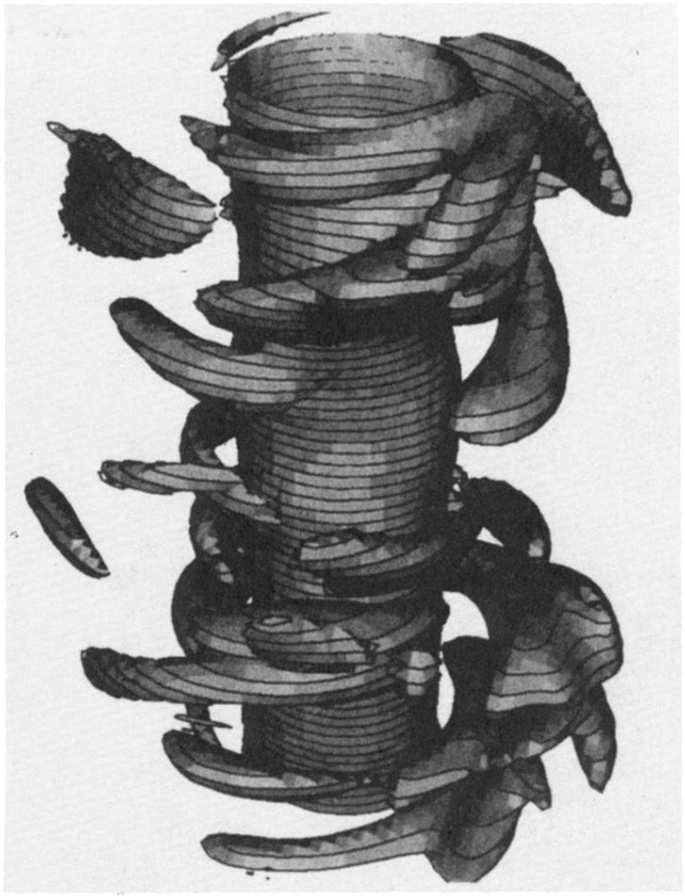

FIG. 5. Isovorticity surface for case $T5$ corresponding to frame (q) of Fig. 3. The vorticity norm on the surface equals 10% of the peak value.

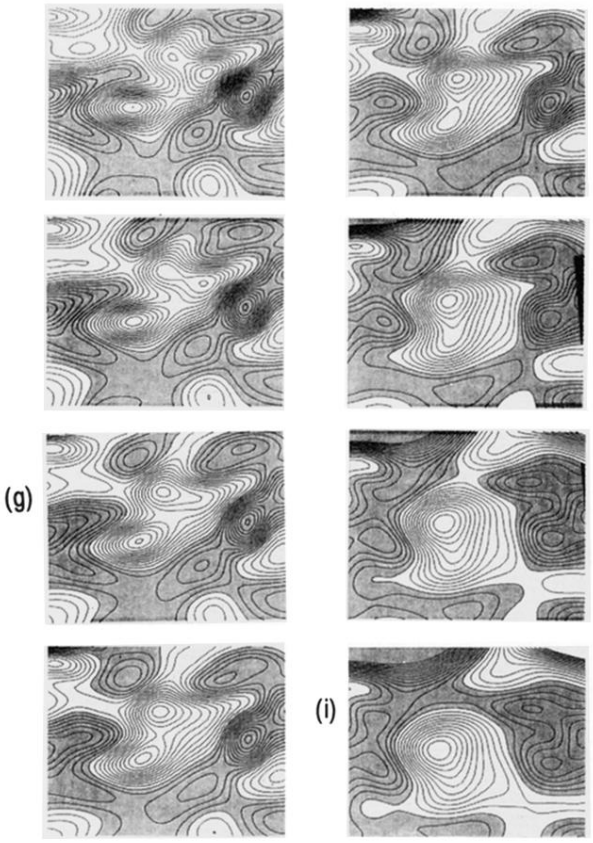

FIG. 8. Enlarged view of a pairing event occurring in simulation $T5$, illustrated by contours of ω_n in $\pi_\parallel$, with negative values shown by gray shading. The enlarged area contains the two small-scale vortical structures indicated by arrows in Fig. 3(g). The successive frames (top to bottom) are at $t^*=2.75$, 2.875, 3.0, 3.125, 3.25, 3.5, 3.75, 4.0.

(A)

(B)

FIG. 9. End result of simulations $T7$ (A) and $T8$ (B), both of which have the flow field in Fig. 3(g) as the starting conditions. The cross sections should be compared with frame (i) of Fig. 8.